




The Complex Space Weather Events of 2017 September

Rajkumar Hajra¹ , Bruce T. Tsurutani², and Gurbax S. Lakhina³

¹ Indian Institute of Technology Indore, Simrol, Indore 453552, India; rajkumarhajra@yahoo.co.in

² Jet Propulsion Laboratory, California Institute of Technology, Pasadena, CA, USA

³ Indian Institute of Geomagnetism, Navi Mumbai 400005, India

Received 2019 November 13; revised 2020 June 21; accepted 2020 June 22; published 2020 August 6

Abstract

Interplanetary coronal mass ejections (ICMEs), magnetic clouds (MCs), sheaths, corotating interaction regions (CIRs), solar wind high-speed streams (HSSs), fast forward shocks (FSs), reverse waves (RWs), stream interfaces, and heliospheric current sheet crossings detected upstream of the Earth and their geoeffectiveness are studied during 2017 September. The most intense geomagnetic storm (SYM-H peak = -146 nT) starting on September 7 had a three-step main phase. A compound interplanetary structure resulting from an FS encountering and compressing the upstream MC southward interplanetary magnetic fields (IMFs) caused the first two steps of the storm. A magnetospheric supersubstorm (SSS; SML peak = -3712 nT) led to the third and most intense step. An MC portion of an ICME created an intense storm (SYM-H peak = -115 nT) on September 8. A second SSS (SML peak = -2642 nT) occurred during the main phase of this storm. Intense geomagnetically induced currents (GICs) occurred during the SSSs. Two moderate magnetic storms with peak SYM-H indices of -65 and -74 nT occurring on September 13 and 27 were caused by sheath and CIR southward IMFs, respectively. Six FSs and their associated sheaths caused sudden impulses (SI⁺s) of magnitude ranging from $+11$ to $+56$ nT. The shocks/sheaths led to magnetospheric relativistic electron flux decreases. The RWs caused SI⁻s and substorm recoveries by reducing southward IMFs. The high-intensity long-duration continuous AE activities (HILDCAAs) caused by the HSSs were related to the increase/acceleration of relativistic electron fluxes.

Unified Astronomy Thesaurus concepts: [Solar flares \(1496\)](#); [Solar coronal mass ejections \(310\)](#); [Corotating streams \(314\)](#); [Interplanetary shocks \(829\)](#);

1. Introduction

The goal of this work is to explore the geoeffectiveness, or lack thereof, of the solar and interplanetary events that occurred during the month of 2017 September, an extremely active solar interval. All of the interplanetary coronal mass ejections (ICMEs), magnetic clouds (MCs), sheaths, corotating interaction regions (CIRs), solar wind high-speed streams (HSSs), stream interfaces (SIs), shocks, reverse waves (RWs), and heliospheric current sheet (HCS)/heliospheric plasma sheet (HPS) crossings detected upstream of the Earth are discussed. By geoeffectiveness, we mean the capability to drive geomagnetic storms, substorms, supersubstorms (SSSs; SML < -2500 nT), high-intensity long-duration continuous auroral electrojet (AE) activities (HILDCAAs), sudden impulses (SI⁺s), geomagnetically induced currents (GICs), and magnetospheric relativistic electron acceleration or flux dropout events.

Although 2017 September was in a descending-to-minimum phase of solar cycle 24, it was characterized by multiple solar and interplanetary events initiated from one solar active region (AR 12673; Chertok et al. 2018; Seaton & Darnel 2018; Augusto et al. 2019; Bruno et al. 2019). A total of 68 CMEs, including four halo events (hCMEs), were detected at the Sun according to the Coordinated Data Analysis Workshops (CDAW) catalog. There were four coronal holes (CHs) emitting HSSs during the interval as well. This multitude of solar activities filled the interplanetary space between the Sun and 1 au.

Extreme solar flares that occurred in 2017 September and their relationships with CMEs have been previously well reported (Attie et al. 2018; Berger et al. 2018; Chamberlin et al. 2018; Chertok et al. 2018; Matthiä et al. 2018; O'Brien et al. 2018; Redmon et al. 2018; Schillings et al. 2018; Yan et al. 2018;

Bruno et al. 2019; Jiggins et al. 2019; Piersanti et al. 2019; Werner et al. 2019; Zou et al. 2019; Scolini et al. 2020). We will summarize some of these relationships below where pertinent to our present work.

In this paper, we will be identifying all of the major interplanetary and geomagnetic events during the month of 2017 September. We will identify not only which solar wind structures were geoeffective but also those that were not, and we will explain why this was the case. This solar activity and the consequential space weather effects are particularly interesting because they have occurred during the late decay phase of the solar cycle.

Fast ICMEs, those propagating faster than the local upstream magnetosonic speed in the plasma frame, can generate upstream shocks followed by sheaths of compressed, heated, and turbulent solar wind plasma and large-amplitude magnetic field variations (e.g., Kennel et al. 1985; Tsurutani et al. 1988). Shocks (and their sheaths), when they impinge on the Earth's magnetosphere, can trigger substorms (Akasofu & Chao 1980; Zhou & Tsurutani 2001; Meurant et al. 2005; Hajra & Tsurutani 2018a). Substorms are one of the end products of the energy coupling between the Sun and the Earth's magnetosphere and ionosphere. During substorms, there is an explosive release of stored magnetotail energy in the form of energetic particles and strong plasma flows (Akasofu 1964, 2017; McPherron 1979; Ohtani 2001; Rostoker 2002; Nykyri et al. 2019, and references therein). This energy is dissipated into the near-Earth nightside auroral region, leading to the excitation of discrete auroras (see Rees 1963, 1964; Semeter & Kamalabadi 2005; Jones et al. 2009; Fang et al. 2010; Artamonov et al. 2016). While substorms were initially believed to be an integral part of magnetic storms (e.g., Akasofu 1964, 1968; Daglis et al. 1994), many studies have reported substorm occurrences

independent of magnetic storms (e.g., Tsurutani & Meng 1972; Tsurutani & Gonzalez 1987; Iyemori & Rao 1996; Hajra et al. 2013, 2014a, 2014b, 2014c, 2015a, 2015b, and references therein). There are also some cases reported of magnetic storms without substorms (e.g., Tsurutani et al. 2003b, 2004b).

Extremely intense substorms or SSSs (Tsurutani et al. 2015; Hajra et al. 2016; Hajra & Tsurutani 2018a) have been speculated to cause GICs at the Earth. The GICs are intense, low-frequency (~ 0.001 – 1 Hz) currents flowing in the ground due to rapid changes of the geomagnetic fields caused by space weather effects (e.g., Campbell 1980; Akasofu & Aspnes 1982; Pirjola 2000; Viljanen et al. 2001; Boteler 2003; Fujita et al. 2016; Pulkkinen et al. 2017; Belakhovsky et al. 2019; Marsal & Torta 2019; Lakhina et al. 2020). They can be damaging to a variety of technological systems, such as electric power systems, natural gas pipelines, and telecommunication cables (e.g., Akasofu & Aspnes 1982; Royal Academy of Engineering Report 2013; Fujita et al. 2016; Pulkkinen et al. 2017, and references therein).

If the interplanetary sheaths contain southward interplanetary magnetic field (IMF) components, they can create magnetic storms (Tsurutani et al. 1988; Zhang et al. 2007; Echer et al. 2008; Meng et al. 2019) through the process of magnetic reconnection (Dungey 1961). It is also well known that the MC (Burlaga et al. 1981; Klein & Burlaga 1982) portion of an ICME can give rise to large storms if the field remains southward for an extended period of time (Gonzalez et al. 1994).

Solar wind HSSs (defined in this paper as ~ 800 km s⁻¹ > $V_{sw} > \sim 550$ km s⁻¹) interacting with upstream slow-speed (~ 350 – 400 km s⁻¹) streams lead to the creation of compressed regions that appear to “corotate” with the Sun, thus their (present) name: CIRs (Davis 1966; Davis et al. 1966; Belcher & Davis 1971; Burlaga 1974; Smith & Wolfe 1976; Gosling et al. 1978; Pizzo 1985; Schwenn 1990; von Steiger et al. 1997; Wimmer-Schweingruber et al. 1997; Balogh et al. 1999; Forsyth & Marsch 1999; Richardson 2018; Allen et al. 2020). Although the gross CIR structure appears to “corotate,” the plasma and fields composing the CIR go almost radially outward from the Sun. This is analogous to a rotating water sprinkler, where the spray streams appear to “corotate” but the water is shot (almost) radially outward. The CIRs are composed of swept-up, compressed, and accelerated slow solar wind on the antisolar side and compressed and decelerated fast solar wind on the solar side. The two regions are separated by a tangential discontinuity called an SI (Belcher & Davis 1971; Burlaga 1974; Hundhausen & Burlaga 1975).

Interplanetary fast forward shocks (FSs) and fast reverse shocks (RSs) can appear on the antisolar and solar edges of the CIRs, respectively (Smith & Wolfe 1976). When these shocks are present, the CIRs are back-to-back sheaths (also with nonshocked plasma located near the SI). The CIRs can cause magnetic storms that are generally weak in intensity because of the highly fluctuating IMF B_z (and southward magnetic fields) therein (Tsurutani et al. 1995).

Large-amplitude Alfvénic fluctuations in an HSS proper (defined as the pure HSS excluding the CIR) can create HILDCAA events (Tsurutani & Gonzalez 1987; Tsurutani et al. 2006a). HILDCAAs have been reported to be associated with the acceleration of magnetospheric relativistic electrons (e.g., Hajra et al. 2014c) in the outer zone radiation belt (Van Allen & Frank 1959). The loss of these relativistic electrons from the magnetosphere has also been ascribed to both interplanetary (e.g.,

West et al. 1972; Tsurutani et al. 2016) and magnetospheric causes (Baker et al. 1994; Horne et al. 2009; Hudson et al. 2014; Hajra & Tsurutani 2018b). HILDCAAs and their relationship to trapped magnetospheric relativistic electrons will also be explored in this paper.

We will study space weather features, from the Sun to the Earth’s ionosphere, for the entire month of 2017 September. In attempting to do this, we will first have to identify the main plasma and magnetic field features in the solar wind and then relate them to the features in the magnetosphere and ionosphere to determine if they are geoeffective or not. The connection of interplanetary phenomena to solar phenomena is much more difficult (e.g., Tsurutani et al. 1988; Tang et al. 1989; Echer et al. 2009). For this, we will rely on other published works and cite them where appropriate.

2. Data and Method of Analysis

Solar Flares

For the intensity and variations of the solar flares during 2017 September, we use the X-ray fluences measured by the Solar X-ray Sensor (XRS) on board the Geostationary Operational Environmental Satellite 15 (GOES 15; Onsager et al. 1996). These data can be found at <https://www.ngdc.noaa.gov/stp/satellite/goes/index.html>.

FSs, RWs, SIs, and HCS Crossings

To study the interplanetary characteristics of the space weather events, the solar wind plasma and IMFs were obtained from the OMNI website (<https://omniweb.gsfc.nasa.gov/>). These data had already been adjusted to take into account the solar wind propagation time from the spacecraft to the Earth’s bow shock. Thus, no further temporal adjustments to the data were made in this study. The IMFs will be displayed in geocentric solar magnetospheric (GSM) coordinates, where the x -axis is directed toward the Sun and the y -axis is in the $\Omega \times \hat{x}/|\Omega \times \hat{x}|$ direction, where Ω is aligned with the magnetic south pole axis of the Earth. The z -axis completes a right-hand system.

To identify the nature of an interplanetary discontinuity that is suspected of being a magnetosonic shock, we calculated the normal vector to the discontinuity and its angle (θ_{Bn}) relative to the upstream IMF. The normal direction is determined using the Abraham–Shrauner (1972) mixed-mode method. To determine if the discontinuity is a fast shock or a magnetosonic wave traveling at subshock speeds, the Rankine–Hugoniot conservation equations are applied to upstream and downstream plasmas and magnetic fields (Smith 1985; Tsurutani & Lin 1985; Tsurutani et al. 2011). The magnetosonic Mach number (MMN) is estimated by comparing the calculated discontinuity speed to the upstream magnetosonic wave speed.

Tangential discontinuities that are HCS crossings are of particular interest, as they have been reported to cause some space weather effects in the magnetosphere. The HCS crossings can be identified by simultaneous polarity reversals of the IMF B_x and B_y components (Ness & Wilcox 1964; Smith et al. 1978; Tsurutani et al. 1995). This corresponds to an IMF azimuthal angular (Φ) change of $\sim 180^\circ$ within a few tens of minutes (see Lepping et al. 1996). A high plasma density region adjacent to the HCS has been named the HPS (Winterhalter et al. 1994; Crooker et al. 2004, 2012).

The SIs are identified by three criteria, namely, an abrupt decrease in solar wind plasma density, a simultaneous increase in proton temperature, and a small increase in solar wind speed

(Burlaga 1974). Gosling et al. (1978) also showed that there is an alpha-to-proton density ratio increase at the SIs. Both sets of criteria will be used by us in our search for SIs in the data set.

CMEs and ICMEs

The coronal mass ejections (CMEs) are observed by the Large Angle and Spectrometric Coronagraph (LASCO) on board the Solar and Heliospheric Observatory (SOHO; Domingo et al. 1995; <https://sohowww.nascom.nasa.gov/>). The CME list presented in this work is collected from the CDAW SOHO/LASCO CME catalog (https://cdaw.gsfc.nasa.gov/CME_list/index.html). A CME at the Sun consists of a bright loop at the outer antisolar extent, a dark region in the middle, and a bright, high-density filament near the base (e.g., Illing & Hundhausen 1986). However, CMEs can be distorted and rotated as they propagate outward from the Sun to 1 au (see, e.g., Odstrcil & Pizzo 1999a, 1999b; Yurchyshyn et al. 2007; Palmerio et al. 2018). Additionally, some of the three CME parts (loop, dark region, and filament) may also detach and not reach 1 au or reach 1 au separately from the other CME parts. For these reasons, a clear distinction has been made between CMEs near the Sun and what is detected at 1 au. The latter have been called ICMEs (Farrugia et al. 1997; Tsurutani & Gonzalez 1997; Zurbuchen & Richardson 2006).

The three parts of a CME are typically not detected together at 1 au (e.g., Burlaga et al. 1981; Tsurutani & Gonzalez 1997; Lepri & Zurbuchen 2010). It may be mentioned that there is only one well-documented event detected at 1 au where all three distinct parts of a CME were detected together: the 1997 January 10 event. At 1 au, the loop was identified by Tsurutani et al. (1998), an MC was identified and will be discussed below, and a filament identified by Burlaga et al. (1998).

A subset of ICMEs is identified as MCs (Burlaga et al. 1981; Klein & Burlaga 1982; Tsurutani & Gonzalez 1997). This is typically the only part of an ICME that is detected at 1 au (Lepri & Zurbuchen 2010). An MC typically has an absence of waves and discontinuities and has an enhanced magnetic field magnitude coupled with reduced proton temperature and low plasma β (β is defined as the ratio of the plasma pressure to the magnetic pressure). It has been argued by Farrugia et al. (1997) and Tsurutani & Gonzalez (1997) that the CME dark regions observed in imaging near the Sun are the MC portions detected at 1 au. In the present work, the MCs are identified based on the observed low β . We do not require the magnetic field rotation (flux rope) described in Burlaga et al. (1981) because one is not certain what part of the MC the spacecraft has crossed. For example, if only the outer extent of a flux rope is crossed, there will not be a clear magnetic field rotation (see schematics in Burlaga et al. 1981; Marubashi 2000; Marubashi & Lepping 2007).

As mentioned earlier, fast ICMEs result in the formation of interplanetary shocks antisunward of the CMEs, followed by downstream (sunward) interplanetary sheaths (Kennel et al. 1985; Tsurutani & Lin 1985; Tsurutani et al. 1988). In the present work, sheaths are identified by compressed, heated, and turbulent solar wind plasma and large-amplitude magnetic field variations following an interplanetary shock.

CHs, HSSs, and CIRs

The solar coronal images taken by the Atmospheric Imaging Assembly (AIA; Lemen et al. 2012) telescope on board the NASA Solar Dynamics Observatory (SDO) are utilized to identify CHs (<https://sdo.gsfc.nasa.gov/>). In addition, we will use the solar synoptic maps prepared by the Space Weather

Prediction Center (SWPC) at the National Oceanic and Atmospheric Administration (<https://www.swpc.noaa.gov/products/solar-synoptic-map>) in order to characterize the CHs.

The solar wind HSSs emanating from the CHs (Krieger et al. 1973; Burlaga et al. 1978; Sheeley & Harvey 1981; Bame et al. 1993) are assumed to have a peak speed of $\sim 750\text{--}800\text{ km s}^{-1}$ (McComas et al. 2000). The lesser speeds of $\sim 550\text{--}750\text{ km s}^{-1}$ are due to superradial expansion at the edges of the HSSs. The core of an HSS from a particular CH can arrive at the Earth within $\sim 2\text{--}3$ days after release from the solar corona. With this assumption, HSSs identified in interplanetary data will be related to CHs observed by SDO/AIA.

The CIRs are identified in the region between HSSs and slow-speed streams as characterized by high plasma densities, temperatures, and magnetic fields.

Magnetic Storms, Substorms, SSSs, HILDCAAs, and GICs

The symmetric ring current SYM-H indices are obtained from the World Data Center for Geomagnetism, Kyoto, Japan (<http://wdc.kugi.kyoto-u.ac.jp/>). These indices will be used to identify and study geomagnetic storms (with the SYM-H peak $< -50\text{ nT}$; Gonzalez et al. 1994). It may be noted that earlier studies like Gonzalez et al. (1994) used the 1 hr resolution disturbance storm time (Dst) indices (e.g., Sugiura 1964; Burton et al. 1975) to define magnetic storms. The more recently developed 1 minute SYM-H indices (see Wanliss & Showalter 2006; Iyemori et al. 2010) have essentially replaced Dst in recent published storm studies (e.g., Echer et al. 2010a; Hajra & Tsurutani 2018a, 2018b; Jin et al. 2018). Although the peak storm intensities in either Dst or SYM-H are almost the same value (Wanliss & Showalter 2006), the high time resolution of the SYM-H index gives more information, a point that will be revisited later in the paper.

HILDCAAs (Tsurutani & Gonzalez 1987) are identified as intervals of (1) high-intensity (peak AE $> 1000\text{ nT}$), (2) long-duration (> 2 days), (3) continuous (no gaps of AE $< 200\text{ nT}$ for 2 hr or more) AE activity (4) occurring during a nonstorm (with SYM-H $> -50\text{ nT}$) interval. In this paper, we will identify HILDCAAs with a somewhat relaxed view of requirement (3).

The auroral SME and SML indices (Gjerloev 2009) indicate auroral activity levels. The indices are based on ~ 300 ground-based magnetometer data taken from the SuperMAG network (<http://supermag.jhuapl.edu/>). Following Newell & Gjerloev (2011), an auroral substorm is defined as an interval of a sharp decrease in the SML index, which presents a proxy for the westward AE current, leading to a negative bay development. This is followed by the bay recovery to pre-substorm values. The SSSs are extremely intense substorms. They are defined in this paper as peak SML $< -2500\text{ nT}$, an arbitrary threshold that has been previously used (Tsurutani et al. 2015; Hajra et al. 2016).

It may be noted that in this paper, we have substituted the SME and SML indices for the AE and AL indices, respectively. Historically, the AE and AL indices are based on geomagnetic field horizontal component observations from 12 geomagnetic stations located around $\sim 60^\circ\text{N}\text{--}70^\circ\text{N}$ (geomagnetic) latitude (see Davis & Sugiura 1966). To overcome the insufficiency of these indices for auroral activities located at very high and/or very low latitudes, the SuperMAG network of ~ 300 ground magnetometers was developed. This network includes, in addition to the standard AE/AL sites, higher- and lower-latitude stations, the latter of which are particularly important during extreme events.

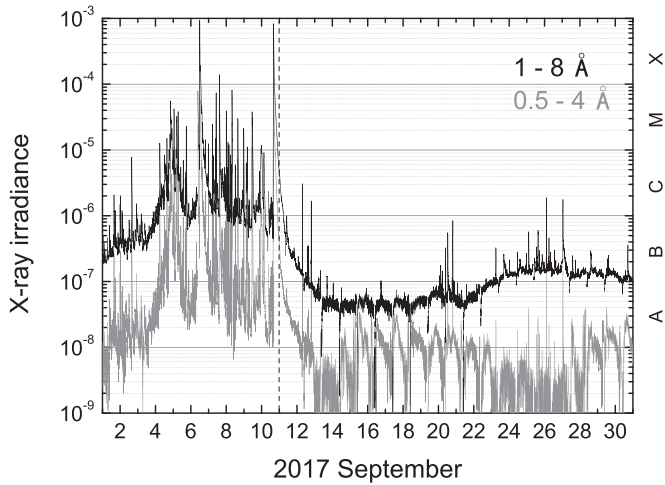


Figure 1. GOES X-ray irradiance (in W m^{-2}) during 2017 September. The x-axis shows the days of 2017 September (in UT). The classes of X-ray flares are indicated on the right. The dashed vertical line indicates the time when AR 12673 rotated over the west limb of the Sun.

The GIC observations used in this study are measured from the natural gas pipeline recordings taken near Mäntsälä, Finland (geographic: 60.6°N , 25.2°E ; Pirjola & Lehtinen 1985; Pulkkinen et al. 2001; Viljanen et al. 2006). These are available from the Space and Earth Observation Centre of the Finnish Meteorological Institute (<https://space.fmi.fi/gic/index.php>).

Relativistic Electrons

To study the outer zone radiation belt dynamics during this month-long space weather interval, variations of the 2.00–7.15 MeV relativistic electron fluxes measured by the Relativistic Electron–Proton Telescope (REPT) instrument on board the NASA Van Allen Probes (VAPs; Kessel et al. 2013; Mauk et al. 2013) are used. The data can be obtained at <http://vanallenprobes.jhuapl.edu/index.php>. The >0.8 and >2.0 MeV electron fluxes measured by the Energetic Proton, Electron, and Alpha Detector (EPEAD) instrument on board GOES 15 stationed at geosynchronous ($L=6.6$) orbit will also be used in this part of the study (<https://www.ngdc.noaa.gov/stp/satellite/goes/index.html>).

3. Results

3.1. Major Solar Flares and CMEs during 2017 September

Flares

Figure 1 shows the GOES/XRS X-ray fluences at 1–8 and 0.5–4 Å wavelength ranges from 2017 September 1 through 30. A large number of solar flares were recorded, of which four were X-class and 27 were M-class flares. The onset of this flare activity was attributed to the extremely rapid development and increasing complexity of AR 12673 on September 4–5 near the central meridian of the Sun (e.g., Chertok et al. 2018; Seaton & Darnel 2018; Augusto et al. 2019). On September 10, the AR rotated over the west limb, and this accounts for the drop-off in the X-ray flux after this time.

The most powerful flares during the interval of study can be noted to occur during September 6–10. The major ($>10^{-4}$ W m^{-2}) X-flare (XFlare) details are listed in Table 1. They are named according to their onset dates. A similar naming scheme is used throughout the paper. The flares occurred when AR 12673 rotated from $\sim\text{W}33$ to $\sim\text{W}88$. The strongest flare of the

Table 1
X-class Solar Flares Recorded during 2017 September

Flare No.	Date	Start Time (UT)	Peak Time (UT)	End Time (UT)	Peak X-Ray Intensity	Location
XFlare_06_1	06/09	08:57	09:10	09:17	X2.2	S07W33
XFlare_06_2	06/09	11:53	12:02	12:10	X9.3	S08W33
XFlare_07	07/09	14:20	14:36	14:55	X1.3	S11W49
XFlare_10	10/09	15:35	16:06	16:31	X8.2	S08W88

Note. The dates are given in day/month format.

Table 2
hCMEs Identified in the CDAW Catalog during 2017 September

CME No.	CME Time (UT)	Associated Flare Intensity
hCME_04	04/09 20:36	M5.5
hCME_06	06/09 12:24	X9.3
hCME_10	10/09 16:00	X8.2
hCME_17	17/09 12:00	Far side

month was XFlare_06_2, which erupted at $\sim 11:53$ UT on September 6 with a peak X-ray intensity of X9.3. It was also the most intense event of solar cycle 24.

CMEs

As mentioned previously, four of the 68 CMEs listed in the SOHO/LASCO CDAW catalog were hCMEs. The hCMEs are listed in Table 2 with their associated flares.

The hCME_04 was associated with an M5.5 flare (started at $\sim 20:28$ UT, attained peak intensity at $\sim 20:33$ UT and ended at $\sim 20:37$ UT) on September 4, hCME_06 was associated with the X9.3 (XFlare_06_2) flare on September 6, and hCME_10 was associated with the X8.2 (XFlare_10) flare on September 10 (Table 1). For hCME_17, launched on September 17, no C-class or higher flare was detected by GOES/XRS. This is because the AR producing the CME had moved to the far side of the Sun relative to the Earth, and any related flare was not detected by the GOES detectors. The hCME_17 did not reach the Earth.

3.2. Interplanetary Structures and Their Geomagnetic Effects During 2017 September: An Overview

Figure 2 shows an overview plot of the solar wind plasma, IMF, and geomagnetic activity variations during 2017 September. The major interplanetary structures are marked. They include 15 major interplanetary discontinuities (marked by vertical lines in the figure), four interplanetary sheaths (green horizontal bars on the top), two MCs (red horizontal bars and vertical purple shading), four solar wind HSSs, and four CIRs (blue horizontal bars). The characteristics of these major discontinuities and interplanetary structures are listed in Tables 3 and 4, respectively. All of the structures are labeled according to their onset dates.

During six of the 15 major discontinuities, the solar wind speed v_{sw} , plasma density n_{sw} , ram pressure P_{sw} , temperature T_{sw} , and IMF amplitude B_0 increased abruptly from the upstream (antisunward) to the downstream (sunward) regions relative to the discontinuities. Rankine–Hugoniot analyses were performed on these intervals. The discontinuities were identified as (magnetosonic) FSs propagating in the antisunward (forward) direction. The FSs are indicated by red solid

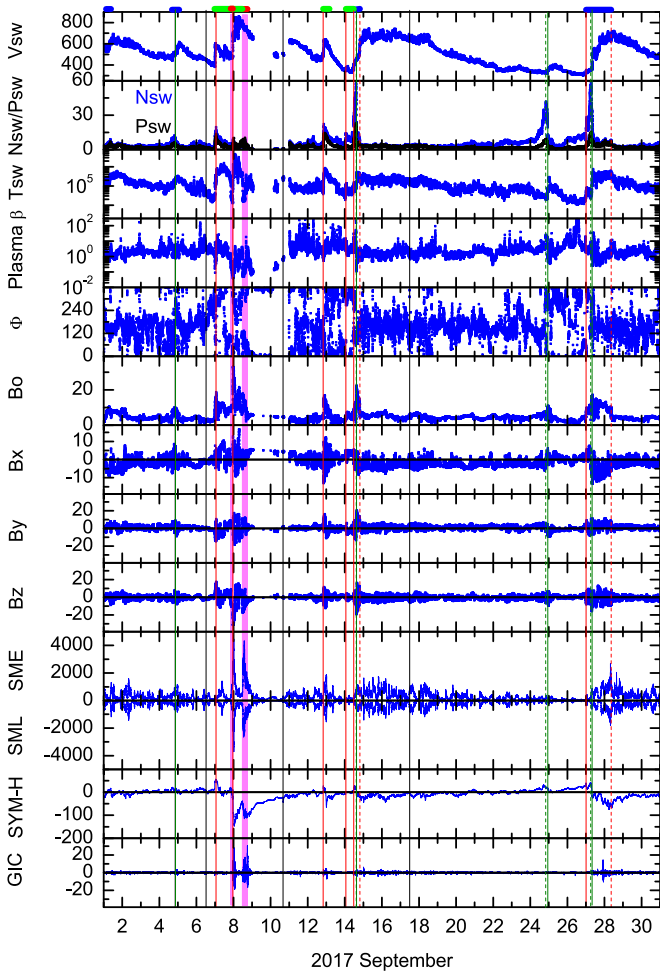


Figure 2. Solar wind/interplanetary and geomagnetic variations during 2017 September. From top to bottom, the panels show the solar wind plasma speed (V_{sw} ; km s^{-1}), density (N_{sw} ; cm^{-3} ; blue) and ram pressure (P_{sw} ; nPa ; black), plasma temperature (T_{sw} ; K), plasma beta (β , defined as the ratio of the plasma pressure to the magnetic pressure), magnetic field azimuthal angle (Φ ; deg), magnetic field (IMF) amplitude B_0 (nT), B_x (nT), B_y (nT) and B_z (nT) components in the GSM coordinate system, AE SME (nT) and SML (nT) indices, symmetric ring current SYM-H index (nT), and GIC (A) at Mäntsälä, Finland. The x-axis shows the days of 2017 September (UT). Vertical lines indicate FSs (red solid), RWs (red dashed), SIs (green solid), HSSs (green dashed), and the times of the frontside hCMEs (black solid). On the top, horizontal bars indicate the interplanetary sheath (green), MC (red), and CIR (blue) intervals. The MCs are also marked by vertical purple shading.

vertical lines in Figure 2. Their detailed properties are given in Table 3. The shocks propagate with speeds larger than the upstream magnetosonic speed; thus, they all have MMNs greater than 1.0 (by definition). The FSs have downstream density compressions that are approximately equal to the Mach number for low Mach number shocks ($\text{MMN} < 4$) and a maximum compression of ~ 4 for high Mach number shocks ($\text{MMN} > 4$; Kennel et al. 1985; Tsurutani et al. 2011). Thus, when a shock/sheath impacts the Earth’s magnetosphere, a strong compression takes place that can lead to several types of different magnetospheric space weather effects.

Two of the 15 discontinuities were characterized by sharp V_{sw} increases and simultaneous N_{sw} , P_{sw} , and T_{sw} decreases. These discontinuities were determined to be moving at submagnetosonic speeds, indicating that they were not shocks. Specifically, they were RWs, by which we mean that the waves were propagating toward the Sun but, because the solar wind

speed was higher than the speed of the waves within the plasma, the waves were convected in the antisunward direction. These two RWs are indicated by red dashed vertical lines in Figure 2 and listed in Table 3.

Among the 15 major discontinuities detected in this study, four were SIs (indicated by green solid vertical lines in Figure 2 and listed in Table 3). These were all found to be tangential discontinuities where the solar wind plasma densities N_{sw} decreased abruptly, accompanied by large increases in temperature T_{sw} and small increases in speed V_{sw} . In addition, abrupt increases in the alpha-to-proton density ratio, from lower values in the slow wind to higher values in the HSSs, are noted at the SIs (not shown).

Three of the SIs were preceded by HCS crossings. These HCS discontinuities are indicated by green dashed vertical lines in Figure 2 and listed in Table 3.

The bottom three panels of Figure 2 show geomagnetic activity indices. The symmetric ring current SYM-H indices indicate occurrences of two intense (SYM-H peak < -100 nT) geomagnetic storms on September 7 and 8 and two moderate (-50 nT $>$ SYM-H peak > -100 nT) storms on September 13 and 27. Intense and moderate substorm activity may be noted in the SME and SML index variations. Two SSSs were detected during September 7–8.

Case-by-case analyses of the interplanetary structures, their characteristics, and their geomagnetic impacts are presented in the following sections.

3.3. Interplanetary Structures and Their Geomagnetic Effects during 2017 September: Case Studies

September 1–5 Events

Figure 3 shows the interplanetary and geomagnetic activity during September 1–5. A small region with compressed plasma density $N_{sw} \sim 7 \text{ cm}^{-3}$ and IMF $B_0 \sim 10$ nT is recorded from $\sim 03:07$ to $\sim 09:22$ UT on September 1 (Table 4). This is CIR_01, marked by a blue horizontal bar at the top of Figure 3. It is followed by the solar wind HSS_01, with a peak plasma speed V_{sw} of $\sim 689 \text{ km s}^{-1}$ at $\sim 12:19$ UT on September 1 (Table 4). The HSS_01 extended to approximately the end of September 2. Based on the HSS_01 speed, this was related to a large CH (labeled with CH25 in the SWPC solar synoptic map) evident in observations from the SDO/AIA telescope on August 28. The CH extended from the solar north pole down to $\sim +5^\circ$ latitude at $\sim 180^\circ$ Carrington longitude on that date (not shown). The CH25 had a “positive” magnetic polarity (defined as the magnetic field pointing away from the Sun). The CH magnetic polarity is consistent with the antisunward IMF direction as observed from negative B_x and positive B_y values (and more directly from Φ). No magnetic storm was recorded in SYM-H (the peak SYM-H was only -28 nT, below the threshold of a geomagnetic storm). Discrete, multiple southward components (IMF $B_z \sim -5$ nT) of an Alfvén wave train embedded within HSS_01 proper resulted in intense auroral activity, with peak SME and SML intensities of ~ 1588 and ~ -1439 nT, respectively, continuing for > 2 days. This is a HILDCAA event.

At the trailing end of HSS_01, a region with a plasma density N_{sw} enhancement from ~ 4 to $\sim 13 \text{ cm}^{-3}$, an IMF B_0 enhancement from ~ 3 to ~ 9 nT can be identified from $\sim 16:19$ to $\sim 01:37$ UT on September 5. This is identified as CIR_04 (Table 4). While no clear shock/wave signatures were

Table 3
Characteristics of the Interplanetary Discontinuities at WIND Spacecraft

Time (UT)	Type	Driver	Jump in Interplanetary Parameters					θ_{Bn} (deg)	MMN
			Vsw (km s ⁻¹)	Nsw (cm ⁻³)	Psw (nPa)	Tsw (10 ⁵ K)	Bo (nT)		
04/09 20:53	SI_04		492–521	10–6					
07/09 00:00	FS_07_1	CME	391–591	4–14	2–9	0.3–1.8	4–13	89.8	5.80
07/09 23:02	FS_07_2	CME	477–708	3–9	1–6	0.2–5.8	10–25	47.9	6.73
12/09 19:55	FS_12	CME	482–536	6–14	3–10	0.4–0.9	4–11	19.4	3.97
14/09 01:26	FS_14_1	CIR	343–373	5–13	1–4	0.3–1.0	3–5	8.5	4.30
14/09 11:31	FS_14_2	CIR	352–390	11–29	3–9	0.7–1.2	4–7	84.0	1.73
14/09 14:50	HCS_14								
14/09 15:07	SI_14		445–458	43–7		1.0–5.4			
14/09 19:26	RW_14	CIR	516–576	8–4	5–3	4.1–2.4	12–8	71.2	0.84
24/09 19:54	HCS_24								
24/09 22:40	SI_24		321–340	29–13		0.3–0.8			
27/09 00:15	FS_27	CIR	315–345	10–20	2–4	0.2–0.6	5–8	33.5	2.72
27/09 06:10	HCS_27								
27/09 07:58	SI_27		358–420	44–19		0.4–1.7			
28/09 08:38	RW_28	CIR	634–680	8–4	7–2	6.2–3.4	10–5	86.7	0.71

identified at the leading and trailing edges of CIR_04, an SI, SI_04, was detected inside CIR_04.

The SI_04 occurred at $\sim 20:53$ UT on September 4 (Table 3). It was characterized by an abrupt Nsw decrease from ~ 10 to 6 cm^{-3} and a Tsw increase from $\sim 1.5 \times 10^5$ to $\sim 2.5 \times 10^5$ K. The Vsw varied slowly from ~ 492 to $\sim 521 \text{ km s}^{-1}$ across SI_04. It separated a slow wind with a low alpha-to-proton density ratio from a fast wind with a higher ratio (not shown). Ahead of SI_04, a peak ram pressure Psw of ~ 5 nPa was recorded. This is followed by a southward IMF Bz of ~ -8 nT. These interplanetary structures led to an intense substorm with peak SME and SML intensities of 1176 and -800 nT, respectively, at $\sim 23:14$ UT on September 4.

The CIR_04 was followed by a short-duration fast stream, HSS_05, that continued until the middle of September 5. The HSS_05 had a peak Vsw of $\sim 620 \text{ km s}^{-1}$ at $\sim 01:46$ UT on September 5. The HSS may be related to CH25, which decreased in size and corotated to the western edge of the Sun on September 2. The Predictive Science mapping tool (http://www.predsci.com/mhdweb/spacecraft_mapping.php) suggests that the connection changed from the equatorward extension of the northern polar CH to the polar CH itself (not shown). Here CIR_04 and HSS_05 did not cause geomagnetic storms.

September 6–10 Events

Figure 4 shows interplanetary structures and associated geomagnetic impacts during 2017 September 6–10. A fast interplanetary shock FS_07_1 (Table 3) occurred at $\sim 00:00$ UT on September 7. According to the CME scoreboard developed at NASA’s Community Coordinated Modeling Center (CCMC; <https://kauai.ccmc.gsfc.nasa.gov/CMEscoreboard/>), FS_07_1 was associated with the hCME_04, which erupted on September 4 (Table 2). Our in situ analyses show that at 1 au, the shock was propagating at ~ 5.8 times the magnetosonic speed in the perpendicular direction ($\theta_{Bn} \sim 90^\circ$) to the ambient IMF. This unusual, purely perpendicular shock, with a ram pressure Psw increase of a factor of ~ 4.5 , caused a very large positive sudden impulse (SI⁺) of $\sim +56$ nT (Figure 4, the SYM-H panel) when it and its sheath impacted the magnetosphere.

The FS_07_1 was followed by a sheath (Sheath_07_1) that extended from $\sim 00:00$ to $\sim 20:24$ UT on September 7 (Table 4). The sheath is marked by a green horizontal bar at the

top of Figure 4. The sheath was characterized by large IMF Bz fluctuations with a peak southward Bz component of ~ -12 nT at 06:48 UT on September 7. The associated SYM-H peak was only -15 nT. An intense substorm with SME and SML peak intensities of 1417 and -1097 nT, respectively, was detected at $\sim 09:05$ UT on September 7.

An MC (MC_07) signature was detected between Sheath_07_1 and the shock FS_07_2 from $\sim 20:24$ to $\sim 23:02$ UT on September 7 (Table 4). The interval is indicated by a red horizontal bar at the top of Figure 4 and by vertical purple shading. The MC was characterized by low Tsw ($\sim 0.16 \times 10^5$ K) and low plasma β (~ 0.06). The MC had a southward IMF Bz peak of ~ -10 nT at $\sim 21:06$ UT on September 7.

A fast shock, FS_07_2, was superposed on the MC_07 southward IMF at $\sim 23:02$ UT on September 7 (Table 3). The FS_07_2 was associated with hCME_06 on September 6 (Table 2) according to the CCMC CME scoreboard. The shock was estimated to be propagating at ~ 6.7 times the magnetosonic speed with an angle of $\sim 48^\circ$ relative to the IMF. The shock caused a factor of ~ 6 increase in Psw, and this led to an SI⁺ of $\sim +11$ nT occurring at $\sim 23:02$ UT.

The FS_07_2 was followed by Sheath_07_2 that extended from $\sim 23:02$ UT on September 7 to $\sim 11:31$ UT on September 8 (Table 4). Sheath_07_2 was characterized by large IMF fluctuations with a peak southward Bz of ~ -31 nT at $\sim 23:31$ UT on September 7.

The above compound structure was found to be geoeffective, leading to an intense magnetic storm (IMS_07) with an SYM-H peak intensity of -146 nT. This was the biggest storm of the interval of this study. Figure 5 shows an enlarged data plot of the September 7–8 magnetic storm with both the 1 minute SYM-H values and the 1 hr Dst values shown. The SYM-H plot indicates that the storm had a three-step main phase development. This three-step feature cannot be observed using the low-resolution Dst indices.

Magnetic reconnection by the MC_07 IMF Bz southward turning at $\sim 20:38$ UT on September 7 caused the SYM-H index to decrease from $+18$ nT at $\sim 20:43$ UT to ~ -31 nT at $\sim 23:00$ UT. This southward IMF turning was the cause of the first step of the storm main phase. The FS_07_2 shock caused

Table 4
Interplanetary Structures

Type	Start Time (UT)	End Time (UT)	Peak IMF Bz (nT)	Vsw (km s ⁻¹)
CIR_01	01/09 03:07	01/09 09:22	-9	520-687
HSS_01	01/09 04:09	02/09 23:18	-7	687
CIR_04	04/09 16:19	05/09 01:37	-8	510-620
HSS_05	05/09 01:55	05/09 13:27	-5	620
Sheath_07_1	07/09 00:00	07/09 20:24	-11	600
MC_07	07/09 20:24	07/09 23:02	-10	520
Sheath_07_2	07/09 23:02	08/09 11:31	-31	890
MC_08	08/09 11:31	08/09 18:00	-17	790
Sheath_12	12/09 19:55	13/09 04:05	-12	640
Sheath_14	14/09 01:26	14/09 11:31	-4	390
CIR_14	14/09 11:31	14/09 19:26	-19	333-743
HSS_14	14/09 19:26	18/09 23:12	-7	743
CIR_27	27/09 00:15	28/09 08:38	-15	315-721
HSS_27	27/09 15:41	29/09 22:16	-4	721

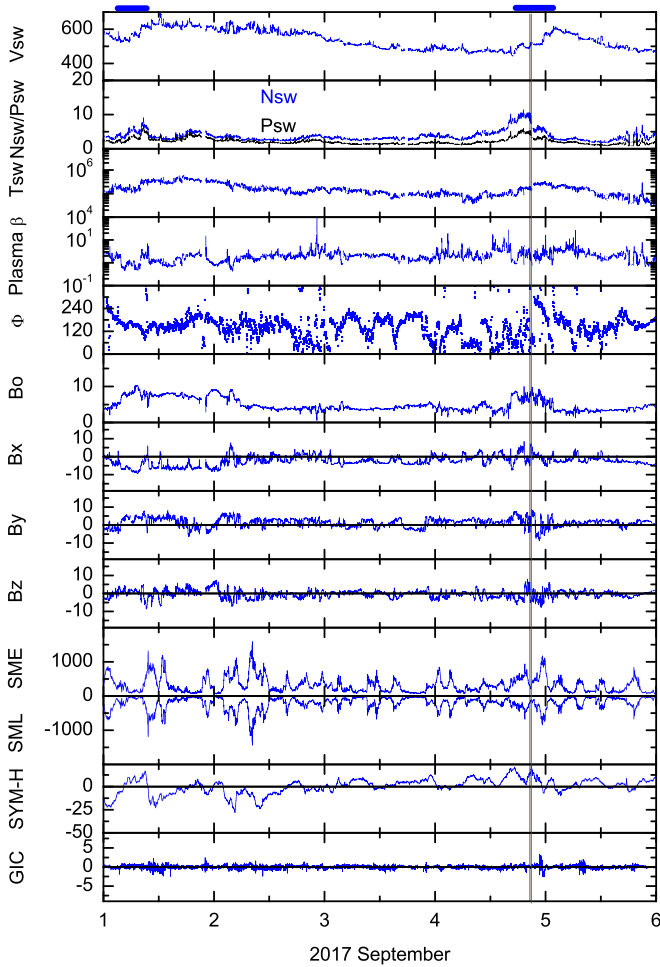


Figure 3. Solar wind/interplanetary and geomagnetic variations during 2017 September 1-5. The panels are in the same format as in Figure 2.

an SI⁺ of $\sim +11$ nT at $\sim 23:30$ UT. The FS_07_2 also produced an enhanced southward IMF in Sheath_07_2 by shock compression. The sheath had a southward Bz peak of -31 nT at 23:31 UT on September 7 that caused a sharp decrease in the SYM-H index to ~ -93 nT at $\sim 23:33$ UT. This stronger sheath southward IMF led to the second step of the storm main phase. The third SYM-H decrease to a peak value

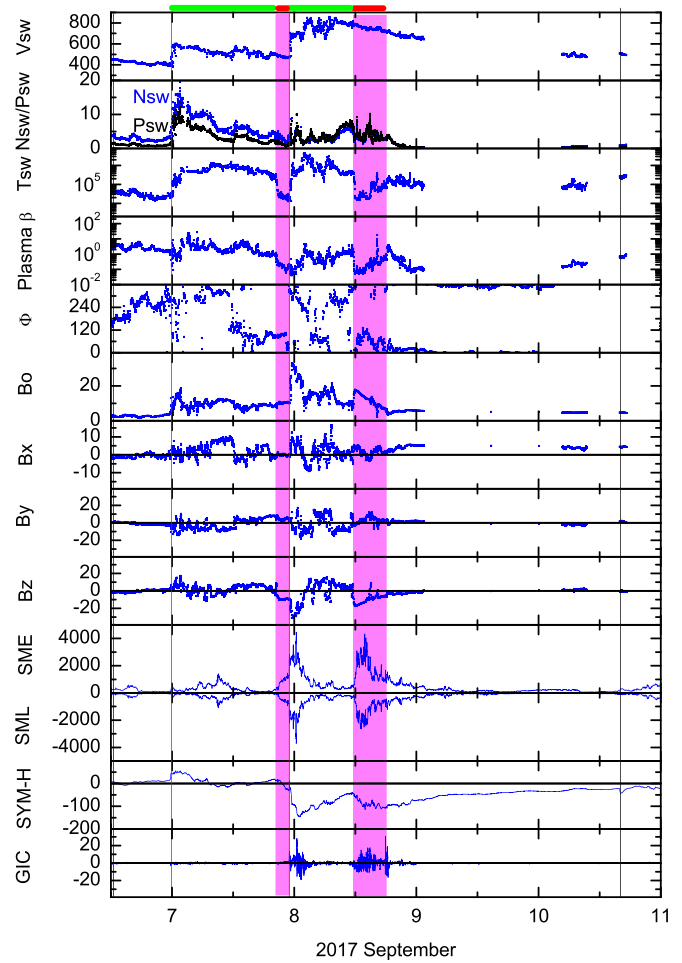


Figure 4. Solar wind/interplanetary and geomagnetic variations during 2017 September 6-10. The panels are in the same format as in Figure 2.

of -146 nT occurred at $\sim 01:08$ UT on September 8. The IMF was southwardly directed but less so than at the second storm step. The third and most intense step of IMS_07 storm main phase development was caused by a long-duration (~ 3 hr 49 minutes), slowly developing SSS (SSS_07). The SSS_07 can be noted in the SME/SML panel of Figure 5 (Table 5). The SSS onset was initiated by the shock (the shock and the SSS

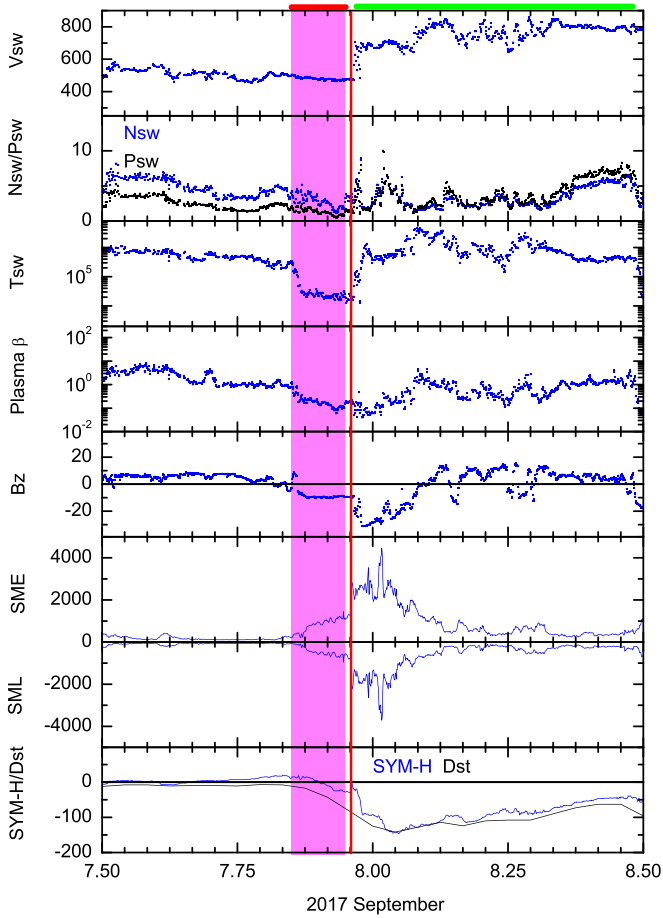


Figure 5. Solar wind/interplanetary and geomagnetic variations for the geomagnetic storm during 2017 September 7–8. From top to bottom, the panels show V_{sw} (km s^{-1}), N_{sw} (cm^{-3} ; blue) and P_{sw} (nPa ; black), T_{sw} (K), plasma β , IMF B_z (nT), SME (nT), SML (nT), and Dst (nT; black) and SYM-H (nT; blue) variations. The x -axis shows the fractional days of 2017 September (UT). The red vertical line indicates an FS. On the top, horizontal red and green bars indicate an MC and a sheath, respectively. The MC is also indicated by vertical purple shading.

onset occurred at the same time). The SSS reached its peak SME and SML intensities of 4464 and -3712 nT, respectively, at $\sim 00:24$ UT on September 8, the time of the onset of the third step of the storm main phase. The SSS₀₇ ended at $\sim 02:51$ UT on September 8.

Very intense GICs were recorded at Mäntsälä during the SSS₀₇ recovery phase. Mäntsälä was in local postmidnight hours. The GICs had a peak eastward intensity of ~ 28 A at $\sim 03:31$ local time (LT = UT + 3 hr).

Sheath_{07_2} was followed by an MC (MC₀₈) that occurred from $\sim 11:31$ through $\sim 18:00$ UT on September 8 (Figure 4, Table 4). This is marked by a red horizontal bar at the top of Figure 4 and vertical purple shading. The MC₀₈ is identified by low β ($\sim 2 \times 10^{-2}$). The MC had a low T_{sw} ($\sim 0.4 \times 10^5$ K), an enhanced magnetic field B_0 (~ 18 nT), and a south-to-zero B_z configuration. The southward IMF component lasted for ~ 3.7 hr with a peak southward B_z intensity of -17 nT at $\sim 11:56$ UT on September 8. This southward B_z was responsible for the development of the main phase of the second intense storm (IMS₀₈) starting at $\sim 11:49$ UT on September 8. This had a peak SYM-H intensity of -115 nT at $13:56$ UT on September 8. This interval was also associated with an SSS (SSS₀₈). The SSS₀₈ started at $\sim 11:34$ UT and

Table 5
SSSs and GICs

SSS No.	SSS Interval		SSS Strength		GIC Impact	
	Start (UT)	End (UT)	SML Peak (nT)	Time (UT)	GIC Peak (A)	Time (LT)
SSS ₀₇	07/09 23:02	08/09 02:51	-3712	08/09 00:24	28.2	08/09 03:31
SSS ₀₈	08/09 11:34	08/09 15:42	-2642	08/09 13:08	30.4	08/09 20:55

ended at $\sim 15:42$ UT on September 8, with a total duration of ~ 4 hr 8 minutes (Table 5). The SSS onset was preceded by an IMF southward turning at $\sim 11:07$ UT as part of MC₀₈. The SSS was characterized by peak SME and SML intensities of 4330 and -2642 nT, respectively, at $\sim 13:08$ UT. Large-amplitude GICs occurred during the SSS₀₈ recovery phase, with a peak (eastward) component of ~ 30 A at $\sim 20:55$ LT at Mäntsälä.

September 12–13 Events

Interplanetary structures and resultant geomagnetic activity during September 12–13 are shown in Figure 6. The fast shock FS₁₂ (Table 3) occurred at $\sim 19:55$ UT on September 12. It was associated with hCME₁₀ on September 10 (Table 2; see the CCMC CME scoreboard). The shock was found to be quasi-parallel in nature with $\theta_{Bn} \sim 19^\circ$, moving with a speed \sim four times the upstream magnetosonic speed. It was characterized by a P_{sw} jump by a factor of ~ 3.3 that caused an SI^+ of $\sim +27$ nT.

The IMFs and plasmas following FS₁₂ indicate a sheath (marked as Sheath₁₂; Table 4) extending from $\sim 19:55$ UT on September 12 to $\sim 04:05$ UT on September 13. This is characterized by large IMF fluctuations with southward B_z components lasting for ~ 25 , ~ 28 , ~ 26 , and ~ 43 minute durations with peak intensities of ~ -8 , ~ -8 , ~ -12 , and ~ -11 nT, respectively. These southward IMFs led to a moderate magnetic storm (MMS₁₂) with an SYM-H peak intensity of -65 nT at $\sim 00:12$ UT on September 13. It may be noted that Sheath₁₂ was not followed by an MC or any ICME signature. The associated hCME₁₀ and XFlare₁₀ erupted from the AR close to the limb. Thus, it is likely that just the flank of the shock was encountered at the Earth and not the ICME/MC, so that only the sheath was detected in this case.

Two intense auroral substorms occurred during this interval. One substorm had peak SME and SML intensities of 1366 and -1071 nT, respectively, at $\sim 21:04$ UT on September 12. Another substorm had peak SME and SML intensities of ~ 1856 and ~ -1541 nT, respectively, at $\sim 23:57$ UT on September 12. The substorms were caused by Sheath₁₂ IMF southward fields.

September 14–16 Events

Figure 7 shows the interplanetary structures during September 13–16 and associated geomagnetic events. The fast shock FS_{14_1} detected at $\sim 01:26$ UT on September 14 was determined to be quasi-parallel, moving at ~ 4.3 times the upstream magnetosonic speed at an angle of $\sim 9^\circ$ relative to the ambient IMF (Table 3). The shock crossing was characterized by a factor of ~ 4 ram pressure P_{sw} jump resulting in $SI^+ \sim +14$ nT.

The FS_{14_1} was followed by an interplanetary sheath region (Sheath₁₄) from $\sim 01:26$ to $\sim 11:31$ UT on September 14 (Table 4). This had only a weak IMF B_z southward

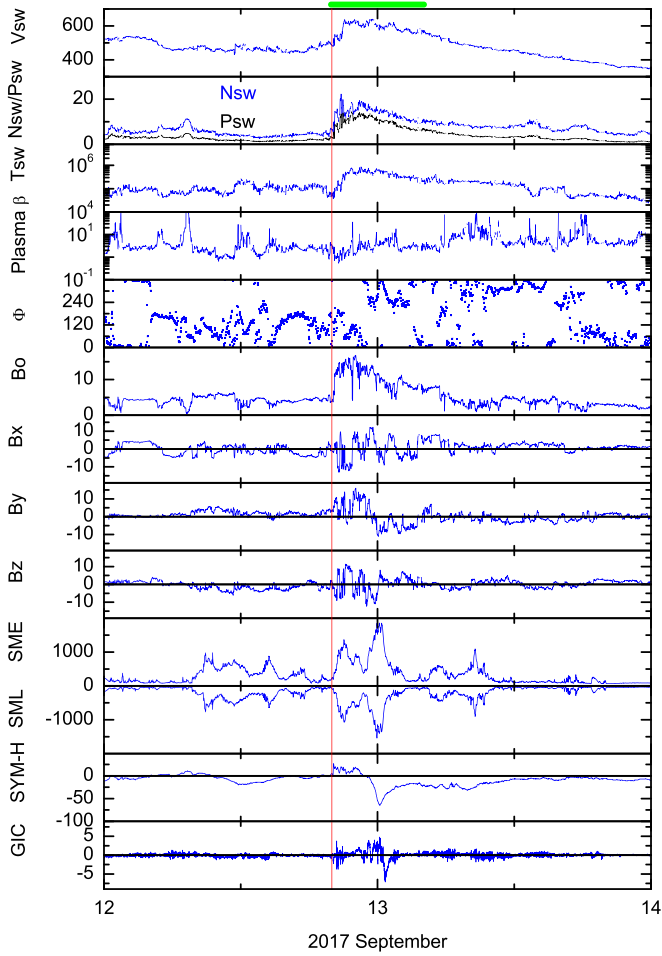


Figure 6. Solar wind/interplanetary and geomagnetic variations during 2017 September 12–13. The panels are in the same format as in Figure 2.

component of ~ -4 nT. While no magnetic storm was detected during this interval, auroral activity had peak SME and SML intensities of 389 and -306 nT, respectively, at $\sim 05:29$ UT on September 14.

Following Sheath₁₄, a CIR (CIR₁₄) was identified extending from $\sim 11:31$ to $\sim 19:26$ UT on September 14 (Table 4). The CIR₁₄ was characterized by a plasma density Nsw enhancement from ~ 6 to ~ 56 cm⁻³ and an IMF Bo enhancement from ~ 2 to ~ 22 nT. The leading and trailing edges of CIR₁₄ were characterized by the fast forward magnetosonic shock FS_{14_2} and the submagnetosonic RW₁₄, respectively (Table 3). In addition, an SI (SI₁₄) was detected within CIR₁₄. The CIR is unusual in that it was previously shown that most CIRs do not have shocks at ~ 1 au (e.g., Tsurutani et al. 1995; Jian et al. 2006). As shock formation through the nonlinear steepening of large-amplitude magnetosonic waves theoretically requires several nonlinear steepening times, shocks are typically expected to form at the leading and trailing edges of the CIRs only at large heliocentric distances (>1.5 – 2.5 au; e.g., Smith & Wolfe 1976). Thus, RW₁₄ is presumably likely to steepen into a shock further from the Sun.

The CIR₁₄ did not cause a magnetic storm (the SYM-H peak was only -19 nT). This was presumably because of the short time durations of the IMF Bz southward components within CIR₁₄. For example, two intervals of southward IMFs

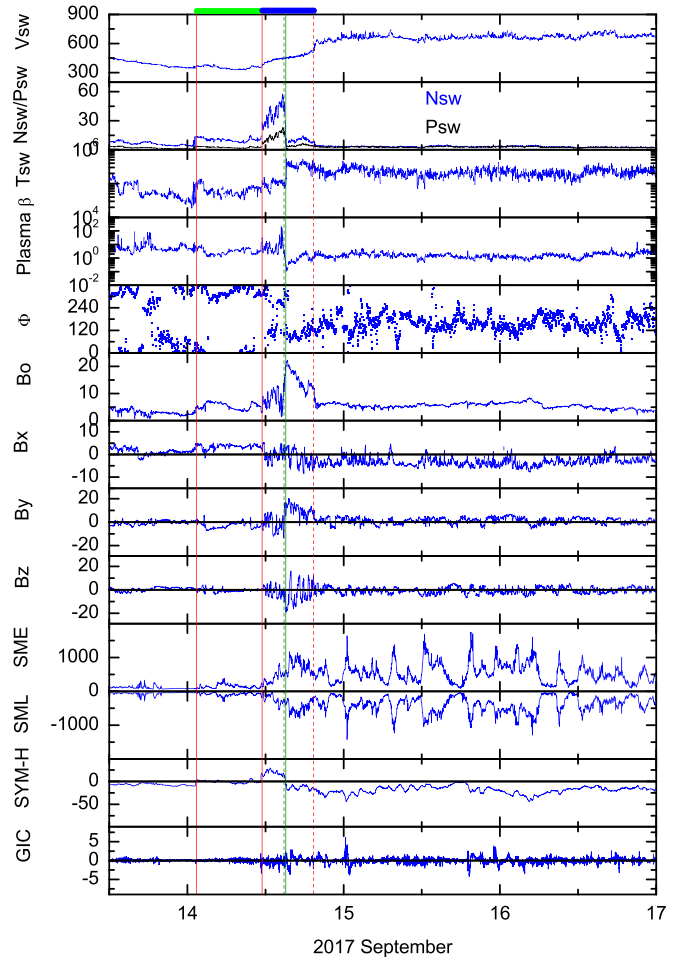


Figure 7. Solar wind/interplanetary and geomagnetic variations during 2017 September 13–16. The panels are in the same format as in Figure 2.

were detected with durations of ~ 38 and ~ 56 minutes and peak Bz of ~ -19 and -16 nT, respectively.

The fast shock FS_{14_2} detected at $\sim 11:31$ UT on September 14 at the CIR₁₄ leading edge was quasi-perpendicular ($\theta_{Bn} \sim 84^\circ$) in nature and a Mach ~ 1.7 shock (Table 3). A ram pressure Psw jump by a factor of ~ 3 led to $SI^+ \sim +28$ nT.

The RW₁₄ at $\sim 19:26$ UT on September 14 at the CIR₁₄ trailing edge was determined to have a speed of $\sim 84\%$ of the upstream (sunward) magnetosonic speed (Table 3). The angle of propagation was $\sim 71^\circ$ relative to the ambient IMF. The ram pressure Psw decreased with time across RW₁₄ to $\sim 60\%$. The RW₁₄ caused a negative sudden impulse (SI⁻) of ~ -23 nT and was also associated with a substorm recovery, as seen from an increase in SML index from a value of ~ -584 nT at $\sim 18:40$ UT to ~ -133 nT at $\sim 19:40$ UT. The weakening of intermittent IMF southward magnetic components (following CIR₁₄) was presumably the cause of the substorm recovery.

An SI (SI₁₄) occurred at $\sim 15:07$ UT on September 14 (Table 3). It was characterized by an abrupt Nsw decrease from ~ 43 to ~ 7 cm⁻³ and a Tsw increase from $\sim 1.0 \times 10^5$ to $\sim 5.4 \times 10^5$ K, when Vsw increased slowly from ~ 445 to ~ 458 km s⁻¹ inside CIR₁₄ (and a prominent increase in the alpha-to-proton density ratio). Energy loading prior to the SI is indicated by an IMF southward turning at $\sim 13:26$ UT. A large ram pressure Psw of ~ 23 nPa adjacent to SI₁₄ impacted the

magnetosphere at $\sim 15:07$ UT and triggered an intense substorm with peak SME and SML intensities of 1171 and -766 nT, respectively, at $\sim 15:41$ UT.

The SI₁₄ was preceded by simultaneous positive-to-negative B_x and negative-to-positive B_y polarity reversals and a Φ change from $\sim 266^\circ$ to $\sim 88^\circ$ occurring in the dense slow solar wind at $\sim 14:50$ UT on September 14. This indicates a large-scale HCS (HCS₁₄) crossing (Table 3).

The CIR₁₄ described above was associated with a solar wind HSS (HSS₁₄) observed from the end of September 14 to the end of September 19. The HSS₁₄ had a peak V_{sw} of ~ 743 km s⁻¹ at $\sim 07:12$ UT on September 15 (Table 4). It emanated from a CH (CH30) on September 12 (the date of the central meridian crossing of the CH center) with positive magnetic polarity. The CH extended from the solar north pole down to $\sim +15^\circ$ latitude with a longitude extending from Carrington $\sim 80^\circ$ to $\sim 240^\circ$. The HSS₁₄ was associated with long-duration IMF B_z fluctuations (the peak southward B_z ~ -6.6 nT), indicating an Alfvén wave train. This Alfvénic interval led to intense and long-duration auroral activity (a HILDCAA event) with peak SME and SML indices of ~ 1749 and -1423 nT, respectively. The SYM-H peak intensity was only -44 nT, indicating that no geomagnetic storm occurred. It may be noted that no significant GIC was recorded during the interval.

September 24–30 Events

The interval from September 24 to 30 is illustrated in Figure 8. An SI (SI₂₄) occurred at $\sim 22:40$ UT on September 24 (Table 3), characterized by an abrupt N_{sw} decrease from ~ 29 to ~ 13 cm⁻³, a T_{sw} increase from $\sim 0.3 \times 10^5$ to $\sim 0.8 \times 10^5$ K, and a slower V_{sw} increase from ~ 321 to ~ 340 km s⁻¹ (with an abrupt increase in the alpha-to-proton density ratio). The SI₂₄ was preceded by simultaneous negative-to-positive B_x and positive-to-negative B_y polarity reversals and an angular change of $\sim 130^\circ$ to $\sim 313^\circ$ in Φ in dense slow plasma at $\sim 19:54$ UT. This indicates an HCS (HCS₂₄) crossing (Table 3). No substorm was observed during SI₂₄. The enhanced/compressed plasma density region ahead of SI₂₄ and enhanced IMF amplitude following it can be interpreted as a CIR. However, it was not followed by an HSS (the peak V_{sw} was only ~ 400 km s⁻¹ at $\sim 08:40$ UT on September 25). From the SDO/AIA telescope observation, a small, negative-polarity CH (CH31) was detected on September 23 that extended from $\sim 15^\circ$ to $\sim 25^\circ$ latitude in the southern hemisphere at $\sim 270^\circ$ Carrington longitude. The CIR structure may thus imply an encounter with the outer edge of the CH31 flow.

A CIR (CIR₂₇) was identified from $\sim 00:15$ UT on September 27 to $\sim 08:38$ UT on September 28 (Table 4). It was characterized by a plasma density N_{sw} increase from ~ 12 cm⁻³ upstream to ~ 59 cm⁻³ downstream. The IMF B₀ increased from ~ 3 to ~ 17 nT. The CIR₂₇ caused a moderate intensity magnetic storm (MMS₂₇). The storm was characterized by a gradual, multistep main phase development with an SYM-H peak intensity of -74 nT at $\sim 05:57$ UT on September 28. The southward IMF was responsible for this moderate storm. For example, southward IMF intervals of ~ 2 , ~ 3.5 , ~ 1.4 , and ~ 1.3 hr were recorded with peak B_z of ~ -15.4 , ~ -11.3 , ~ -10.5 , and ~ -9.5 nT, respectively, inside CIR₂₇. During the storm main phase, peak SME and SML intensities were 2683 and -1813 nT, respectively.

A shock FS₂₇, and a wave RW₂₈, were located at the leading and trailing edges of CIR₂₇, respectively (Table 3). In addition, an SI, SI₂₇, was detected inside CIR₂₇ at $\sim 07:58$ UT

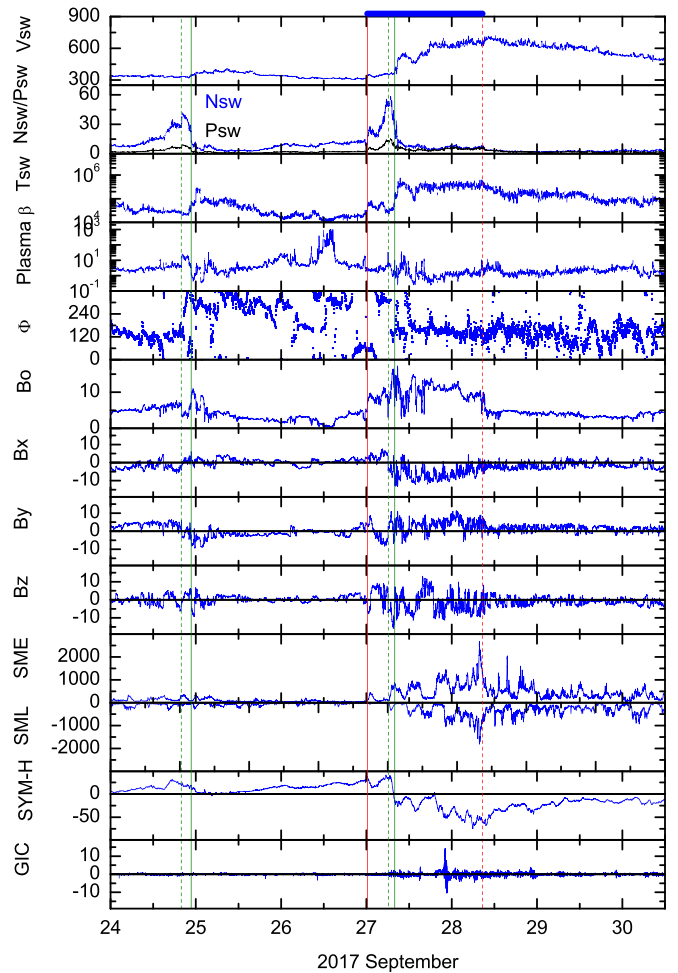


Figure 8. Solar wind/interplanetary and geomagnetic variations during 2017 September 24–30. The panels are in the same format as in Figure 2.

on September 27 (Table 3). The SI₂₇ separated a dense (N_{sw} ~ 55 cm⁻³), cold (T_{sw} $\sim 0.2 \times 10^5$ K) plasma region from a hot (T_{sw} $\sim 1.7 \times 10^5$ K), low-density (N_{sw} ~ 6 cm⁻³) solar wind plasma stream. A characteristic alpha-to-proton density ratio increase was recorded at the SI (not shown). The SI₂₇ was preceded by an HCS (HCS₂₇) crossing with simultaneous positive-to-negative B_x and negative-to-positive B_y polarity reversal and a Φ change from $\sim 314^\circ$ to $\sim 129^\circ$ in slow dense plasma at $\sim 06:10$ UT (Table 3). The SI/HCS was preceded by an enhanced ram pressure P_{sw} of ~ 16 nPa. An episode of southward IMF following SI₂₇ resulted in a substorm with peak SME and SML intensities of 883 and -614 nT, respectively, at $\sim 07:39$ UT on September 27.

The fast shock FS₂₇ detected at the CIR₂₇ leading edge (at $\sim 00:15$ UT on September 27) was determined to propagate at ~ 2.7 times the upstream magnetosonic speed at an angle of $\sim 34^\circ$ relative to the ambient IMF (Table 3). An SI⁺ of $\sim +14$ nT was induced by the shock and its sheath. The ram pressure P_{sw} jump across this shock was ~ 2.0 .

The RW₂₈ at the CIR₂₇ trailing edge (at $\sim 08:38$ UT on September 28) had a speed of $\sim 71\%$ of the upstream magnetosonic speed (Table 3). The wave was propagating nearly perpendicular to the ambient IMF at an angle of $\sim 87^\circ$. The ram pressure P_{sw} decreased to $\sim 29\%$ of its preceding value across RW₂₈. It caused an SI⁻ of ~ -14 nT at $\sim 09:37$ UT on September 28. The RW₂₈ was associated with a significant

weakening of southward IMFs following CIR_27, leading to a substorm recovery phase as seen in an SML decrease from ~ -813 nT at $\sim 09:31$ UT to ~ -198 nT at $\sim 10:04$ UT.

Following CIR_27, a solar wind HSS_27 impacted the Earth's magnetosphere from September 27 to 29 (Table 4). The HSS_27 is the recurrence of the fast stream HSS_01. As a source of this HSS_27, a positive magnetic field CH (CH32) was detected on September 26 (extending from the north pole of the Sun down to $\sim -10^\circ$ latitude at around $\sim 190^\circ$ Carrington longitude). The HSS_27 had a peak V_{sw} of ~ 716 km s^{-1} at $\sim 10:18$ UT on September 28. The HSS_27 proper was characterized by Alfvén wave IMF southward fields (peak B_z of ~ -4 nT). This led to intense and long-duration auroral activity (peak SME ~ 2044 nT, SML ~ -949 nT). The SYM-H peak during HSS_27 was only -43 nT and therefore not a magnetic storm.

3.4. Outer Zone Radiation Belt Variation

The response of the outer zone radiation belt to the complex and multiple space weather events during September 1 through 30 is shown in Figure 9. The figure gives the fluxes of relativistic electrons with energy >0.8 and >2.0 MeV obtained from GOES 15 at geosynchronous orbit ($L = 6.6$; Figure 9, fifth panel from the top) along with the L -shell variations of 2.00–7.15 MeV electron fluxes measured by the REPT instrument on the VAPs (Figure 9, bottom six panels). The top four panels of Figure 9 repeat some of the parameters that have already been mentioned. It may be noted that in Figure 9, the onset times of FSs, RWs, SIs, HCS crossings, and hCMEs are shown by vertical black solid, black dashed, green solid, green dashed, and red solid lines, respectively. The discussion below will be ordered by interplanetary structure type.

Effects of Discontinuities on Relativistic Electron Fluxes

Figure 9 shows that at the GOES 15 geosynchronous orbit, the interplanetary shock FS_07_1 and its sheath were associated with relativistic >0.8 and >2.0 MeV electron flux decreases by ~ 1 order of magnitude followed by a further ~ 1 order of magnitude decrease following the fast shock FS_07_2/sheath impingement on the magnetosphere. The combination of the two shocks and associated sheaths resulted in a net flux decrease of ~ 2 orders of magnitude, from $\sim 990 \times 10^2$ to ~ 450 $cm^{-2} sr^{-1} s^{-1}$ for >0.8 MeV electrons and from $\sim 90 \times 10^2$ to ~ 90 $cm^{-2} sr^{-1} s^{-1}$ for >2.0 MeV electrons. These flux decreases occurred during the main phase of the intense storms of September 7–8. The VAP observations ordered by L -shell show that the entire outer radiation belt was depleted of relativistic electron fluxes during this interval. The flux depletions were most prominent around $L \sim 4-5$ for the 2–4.50 MeV electrons.

The combination of fast shocks FS_12, FS_14_1, and FS_14_2; the interfaces SI_14; and associated sheaths depleted the outer zone radiation belt during September 13–14. At geosynchronous orbit, the net flux decrease was ~ 2 orders of magnitude. The VAP observations show that the L -shell dependence of the flux depletions was energy-dependent. The strongest flux depletions were recorded at $L > 5$ for 2–2.30 MeV electrons, $L > 4.5$ for 2.85 MeV electrons, and $L > 4$ for ≥ 3.60 MeV electrons. No prominent magnetospheric impacts of RW_14 were apparent.

The outer zone ($L > 4$) magnetospheric relativistic electron belt was strongly depleted following SI_24, FS_27, SI_27, and associated interplanetary conditions during September 25–28. No prominent impacts were recorded owing to RW_28.

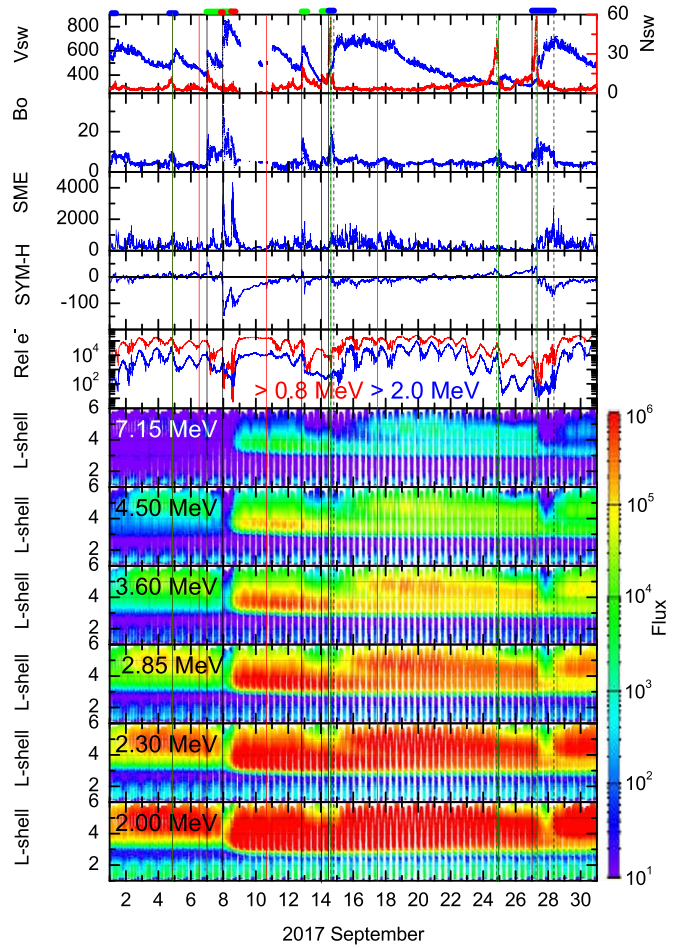


Figure 9. Response of the outer zone radiation belt relativistic electron fluxes to the complex and multiple space weather events. In the top four panels, interplanetary and geomagnetic data from Figure 2 are repeated to give reference to interplanetary and geomagnetic events. The fifth panel from the top displays relativistic >0.8 and >2.0 MeV electron fluxes (in $cm^{-2} sr^{-1} s^{-1}$) obtained from GOES 15 at geosynchronous orbit. The bottom six panels show the L -shell variations of 7.15, 4.50, 3.60, 2.85, 2.30, and 2.00 MeV electron fluxes ($cm^{-2} sr^{-1} s^{-1} MeV^{-1}$) measured by the REPT instrument on the VAPs, respectively. Flux values are indicated by the color scale on the right. Vertical lines indicate FSs (black solid), RWs (black dashed), SIs (green solid), HCSs (green dashed), and the times of the frontside hCMEs (red solid). At the top, horizontal bars indicate the interplanetary sheath (green), MC (red), and CIR (blue) intervals.

Effects of MCs on Relativistic Electron Fluxes

The MC_08 and the magnetic storm (IMS_07) it induced were associated with large relativistic electron flux increases compared to preshock flux values. These increases were mainly at $L < 5$. These results are in agreement with previous findings (Baker et al. 2014; Kanekal et al. 2015). Presumably, the storm time convection electric field injected the energetic $\sim 30-300$ keV electrons deep into the magnetosphere with further particle energization by chorus wave interactions (see, e.g., Horne & Thorne 1998; Reeves et al. 2013; Boyd et al. 2014). Flux enhancements by >2 orders of magnitude were noted around $L \sim 3-4$ associated with the magnetic storm. Most interestingly, the low flux density slot region (typically $2 < L < 2.5$) separating the inner ($L < 2$) and outer ($L > 2.5$) radiation belts moved inward. The large-amplitude flux enhancement during the storm recovery phase is interesting. This was characterized by intense auroral SME/SML substorm activity preceded by an SSS (SSS_08). Thus, this portion is most likely acceleration by chorus

wave interactions with ~ 100 keV electrons (e.g., Horne & Thorne 1998; Summers et al. 2007) associated with the HSS Alfvénic Bz fluctuations creating HILDCAA conditions.

Effects of HSSs on Relativistic Electron Fluxes

The solar wind HSSs (HSS_01, HSS_05, HSS_14, and HSS_27) were associated with repopulating the radiation belt with >0.8 – 7.15 MeV electrons. The largest flux enhancements were recorded around $L \sim 4$ – 5.5 . It may be recollected that peak flux enhancements due to MC_08 were driven deeper into the magnetosphere to $L \sim 3$ – 4 . For the 2.85 – 7.15 MeV electrons, two separated belts can be identified during September 16–27: a radiation belt enhanced by MC_08 around $L \sim 3$ – 3.5 and an enhanced belt due to HSS_14 around $L \sim 4$ – 5 .

4. Summary

We have studied the solar, interplanetary, and geomagnetic events and their interrelationships occurring during 2017 September. This interval was in the descending-to-minimum phase of solar cycle 24. The main results are summarized below.

1. The southward IMF Bz associated with MC_07 led to the first step of a three-step main phase magnetic storm (onset on September 7). A fast forward interplanetary shock, FS_07_2, compressed the MC_07 southward IMFs, resulting in a strong sheath (Sheath_07_2) with a peak IMF Bz of -31 nT (Figures 4 and 5, Table 4). The shock/sheath MC intensification of the IMFs led to the second step of the storm (Figure 5). The FS_07_2 also triggered a slowly developing SSS (SSS_07) that peaked ~ 1 hr 22 minutes after initiation (Table 5). The peak SML value was -3712 nT at $\sim 00:24$ UT on September 8. This SSS caused the third and largest step in the storm main phase, giving a storm peak intensity of SYM-H = -146 nT.
2. On September 8, there was another intense storm (SYM-H peak = -115 nT) caused by southward fields in the MC portion (MC_08) of an hCME (hCME_06; Figure 4, Table 4). Two moderate storms starting on September 13 and 27 with peak SYM-H indices of -65 and -74 nT were caused by southward IMFs associated with a sheath (Sheath_12) and a CIR (CIR_27), respectively (Figures 6 and 8, Table 4).
3. The MC_08 southward magnetic fields and following storm led to relativistic flux enhancements deep within the magnetosphere ($L \sim 3$ – 4 ; Figure 9). In addition, the low flux density slot region ($2 < L < 2.5$) separating the inner ($L < 2$) and outer ($L > 2.5$) radiation belts moved inward to lower L .
4. Six fast forward magnetosonic shocks were detected (Figure 2, Table 3). Half of them were associated with ICMEs, and half were detected at the leading antisunward edges of CIRs. The angle of propagation (θ_{Bn}) of the ICME-driven (CIR-driven) FSs varied from $\sim 19^\circ$ to $\sim 90^\circ$ ($\sim 9^\circ$ to $\sim 84^\circ$) relative to the ambient IMF directions, while their strengths varied from Mach ~ 4.0 to ~ 6.7 (~ 1.7 to ~ 4.3). These are unusually high Mach numbers for interplanetary shocks (Tsurutani & Lin 1985; Echer et al. 2010b). The induced SI^+ s varied between $\sim +11$ and $\sim +56$ nT. Two ICME FSs and sheaths were associated with the onset/trigging of substorms. The FS and sheath impingements led to large MeV electron flux depletions in the Earth's outer radiation belt ($L > 4$; Figure 9).
5. Two nonshock RWs were detected at the trailing edges of the CIRs (Figure 2, Table 3). They were found to be propagating mostly across the magnetic field ($\theta_{Bn} \sim 71^\circ$ – 87°) at submagnetosonic speeds ($\sim 71\%$ – 82% of the magnetosonic speeds). The RWs caused $SI^- \sim -14$ and -23 nT. The RWs were associated with the weakening of the intermittent southward IMFs, leading to the termination of ongoing substorms. There were no reverse shocks detected in this study.
6. Four large-scale SIs were detected (Figure 2, Table 3). The impingement of the high plasma densities associated with the interplanetary structures effectively led to relativistic electron flux decreases in the outer radiation belt.
7. Two SSSs (with peak SML intensities of -3712 and -2642 nT) occurred in the main phases of the two intense magnetic storms (Figure 4, Table 5). The SSSs were preceded (~ 2.8 and ~ 1.1 hr) by precursor southward IMFs followed by solar wind ram pressure pulse triggering. The SSSs were associated with large GICs with peak values of ~ 28 and ~ 30 A recorded at Mäntsälä (Finland) in the local postmidnight and dusk sectors, respectively.
8. Weak and short-duration southward IMFs in a CIR led to a moderate magnetic storm with an SYM-H peak of -74 nT (Figure 8, Table 4). However, three other CIRs did not lead to magnetic storms, but small ring current activity and high-intensity levels of auroral zone activity (peak SME > 1000 nT) during these intervals were noted.
9. The solar wind HSSs led to the HILDCAAs indicated by the SME and SML indices. The HSSs were prominently associated with relativistic electron flux enhancements around $L \sim 4$ – 5.5 (Figure 9).

5. Discussion

During 2017 September, the most intense geomagnetic storm (onset on September 7) had a three-step main phase development with a peak SYM-H intensity of -146 nT. The storm initiation was caused by an ~ -10 nT IMF southward component associated with an MC. The second step was caused by a compound interplanetary structure owing partially to the interaction between an interplanetary FS/sheath and the MC southward IMFs. The shock increased the solar wind ram pressure by a factor of ~ 6.0 , which led to the compression of the upstream MC Bz field to a peak value of ~ -31 nT. This led to the second step of the storm main phase.

For the third and most intense step, there was no obvious IMF southward strengthening. Where did the energy for this storm intensification come from? The FS triggered an SSS with an SML peak intensity of -3712 nT and a long expansive phase of ~ 1 hr 22 minutes. The third and most intense step of the magnetic storm was powered by this SSS, which presumably injected a substantial flux of energetic particles into the ring current. A substorm in general is an explosive release of stored magnetotail energy in the form of energetic particles and strong plasma flows (Akasofu 1964, 2017; McPherron 1979; Ohtani 2001; Rostoker 2002; Nykyri et al. 2019). Thus, we propose that the energy for the

magnetic storm peak came from the SSS that occurred during this phase.

Given that the above scenario is the correct one for the third and major step of the magnetic storm main phase, it should be mentioned that the southward IMF of the MC and its shock compression (and solar wind ram energy) supply the solar wind energy to the magnetosphere/magnetotail (through magnetic reconnection) for all three steps of the magnetic storm. In this scenario, the solar wind energy is transferred to the magnetosphere/magnetotail during the first two intervals of southward IMF. This creates the first two steps of the magnetic storm main phase by direct energy injection. The energy for the third step (due to the SSS) has been stored during the first two storm steps and is delayed with the peak energy injection some hours later.

Portions of the September 7 magnetic storm have been discussed by other authors (e.g., Chertok et al. 2018; Bruno et al. 2019; Scolini et al. 2020). However, all of the cited authors used the low-resolution (1 hr) Dst index to describe the geomagnetic storm. Thus, they failed to identify the three-step main phase development of the storm, and the description of complex interplanetary causes was incomplete. We realize that the above authors cited the magnetic storm only to provide context for their solar studies. However, we encourage solar, interplanetary, and magnetospheric workers that discuss magnetic storms in the future to use the 1 minute resolution SYM-H index instead.

Chertok et al. (2018) reported, “because the second ICME overtook the trailing part of the first ICME near Earth, the resulting Bz component was more intense and southern.” This statement is only partially correct. The shock and sheath that are formed by a fast ICME are not part of the ICME proper (please see Illing & Hundhausen 1986 for a description of CME properties near the Sun discussed earlier in the paper). The sheath is composed of slow solar winds that have been shocked and swept up as the CME shock first forms some distance away from the Sun (Tsurutani et al. 2003a) and then propagates to 1 au. Thus, the properties of the plasma and magnetic fields within a sheath are significantly different than those within the ICME proper.

Bruno et al. (2019) very nicely covered the solar energetic particle events and ground-level enhancements for cases in early 2017 September. These space weather topics were not covered here. Bruno et al. mentioned that the intense southward fields were created by the shock propagating through an upstream ICME. However, Bruno et al. did not perform the Rankine–Hugoniot calculations to prove that the specified interplanetary discontinuity was a shock. Our work has indicated that this was indeed a strong, oblique FS.

Scolini et al. (2020) did particularly nice work not only describing the “CME–CME interaction” of the complex structure that caused the September 7 major magnetic storm but also using simulations to study the time evolution of this interplanetary interaction from closer to the Sun to beyond Earth distance. We highly recommend that the readership of the *Astrophysical Journal* read/study this paper.

However, by our definition, this was not a CME–CME interaction, as stated by Scolini et al. (2020). It is known that there are “slow” ICMEs (those with $V_{sw} < 400 \text{ km s}^{-1}$) detected at 1 au (Tsurutani et al. 2004a). Slow ICMEs have been shown to cause major magnetic storms. Those slow ICMEs that propagate at speeds less than the upstream magnetosonic wave speeds will not have shocks or sheaths.

Therefore, it is also possible to have direct “ICME–ICME interactions.” It is also possible to have direct CME–CME interactions close to the Sun before shocks have formed, as mentioned earlier (Tsurutani et al. 2003a). Although the term “CME–CME interaction” used by Scolini et al. (2020) gives the general idea of the interaction, we prefer a more correct description, “shock/sheath–MC interaction,” which is more specific, and we therefore use this description here. It is possible that in the future, slow MC–slow MC interactions in interplanetary space or CME–CME interactions close to the Sun will be discovered that may lead to confusion in the literature.

In conclusion, this study shows that even near solar minimum, solar events and associated geomagnetic activity can occasionally be particularly complex, with both transients and corotating structures present. The CIRs and solar wind HSSs can lead to a substantial increase in auroral zone geomagnetic activity, particularly in the form of HILDCAAs. Several of these events were noted in this paper. It has previously been shown (Kozyra et al. 2006; Turner et al. 2006; Gonzalez et al. 2006; Tsurutani et al. 2006b; Hajra et al. 2014a) that a 3–4 day interval of a HILDCAA event injects more energy into the magnetosphere/ionosphere system than does a magnetic storm during solar maximum.

During 2017 September, we had HILDCAA-, ICME (MC)-, and sheath-related geomagnetic activity. The HILDCAAs presumably caused the acceleration of relativistic electrons from chorus wave–particle interactions. Magnetic storms caused by sheaths or MC southward IMFs caused relativistic electron acceleration by deep convection into the magnetosphere. Both types of electron energization were evident in the interval of this study.

Abbreviations of Scientific Terms

AE: auroral electrojet index
 AIA: Atmospheric Imaging Assembly
 AL: auroral electrojet (lower trace)
 AR: active region
 au: astronomical unit
 β : plasma beta
 CH: coronal hole
 CIR: corotating interaction region
 CME: coronal mass ejection
 Dst: disturbance storm time
 FS: forward shock
 GIC: geomagnetically induced current
 GSM: geocentric solar magnetospheric
 hCME: halo coronal mass ejection
 HCS: heliospheric current sheet
 HILDCAA: high-intensity long-duration continuous AE activity
 HPS: heliospheric plasma sheet
 HSS: high-speed streams
 ICME: interplanetary coronal mass ejection
 IMF: interplanetary magnetic field
 LT: local time
 MC: magnetic cloud
 MMN: magnetosonic Mach number
 RW: reverse wave
 SI: stream interface
 SI⁺: positive sudden impulse
 SI⁻: negative sudden impulse
 SME: SuperMAG AE

SML: SuperMAG AL
 SSS: supersubstorm
 SYM-H: longitudinally SYMmetric Horizontal component disturbances
 θ_{Bn} : angle of the interplanetary normal vector relative to the upstream IMF
 UT: universal time
 XFlare: X-class flare

The work of R.H. is funded by the Science & Engineering Research Board (SERB), a statutory body of the Department of Science & Technology (DST), Government of India, through a Ramanujan Fellowship. Portions of this work were performed at the Jet Propulsion Laboratory, California Institute of Technology, under contract with NASA. The B.T.T. effort benefited from the discussions in the framework of (or during) the ISSI and the ISSI-BJ project “Relativistic Electron Precipitation and its Atmospheric Effect.” G.S.L. thanks the Indian National Science Academy, New Delhi, for support under the INSA-Honorary Scientist Scheme. The solar X-ray fluences measured by the GOES/XRS are collected from <https://www.ngdc.noaa.gov/stp/satellite/goes/index.html>. The CDAW SOHO/LASCO CME information is available at https://cdaw.gsfc.nasa.gov/CME_list/index.html. The SDO/AIA CH images are obtained from <https://sdo.gsfc.nasa.gov/>. The SWPC solar synoptic maps of CHs are obtained from <https://www.swpc.noaa.gov/products/solar-synoptic-map>. The solar wind plasma and IMFs are obtained from the OMNI website (<https://omniweb.gsfc.nasa.gov/>). The symmetric ring current SYM-H indices are obtained from the World Data Center for Geomagnetism, Kyoto, Japan, at <http://wdc.kugi.kyoto-u.ac.jp/>. The auroral SME and SML indices are taken from the SuperMAG website: <http://supermag.jhuapl.edu/>. The GICs measured in the natural gas pipeline near Mäntsälä, Finland, are available from the Space and Earth Observation Centre of the Finnish Meteorological Institute at <https://space.fmi.fi/gic/index.php>. The NASA Van Allen Probes data are obtained from <http://vanallenprobes.jhuapl.edu/index.php>. The GOES relativistic electron data are collected from <https://www.ngdc.noaa.gov/stp/satellite/goes/index.html>. We would like to thank the reviewer for extremely valuable suggestions that substantially improved the manuscript.

ORCID iDs

Rajkumar Hajra  <https://orcid.org/0000-0003-0447-1531>

References

- Abraham-Shrauner, B. 1972, *JGR*, **77**, 736
 Akasofu, S. I. 1964, *P&SS*, **12**, 273
 Akasofu, S. I. 1968, Polar and Magnetospheric Substorms, Vol. 11 (1st ed.; Netherlands: Springer)
 Akasofu, S. I. 2017, *SSRv*, **212**, 341
 Akasofu, S. I., & Aspnes, J. D. 1982, *Natur*, **295**, 136
 Akasofu, S. I., & Chao, J. K. 1980, *P&SS*, **28**, 381
 Allen, R. C., Lario, D., Odstreil, D., et al. 2020, *ApJS*, **246**, 36
 Artamonov, A. A., Mishev, A. L., & Usoskin, I. G. 2016, *JASTP*, **149**, 161
 Attie, R., Kirk, M. S., Thompson, B. J., Muglach, K., & Norton, A. 2018, *SpWea*, **16**, 1143
 Augusto, C. R. A., Navia, C. E., de Oliveira, M. N., et al. 2019, *PASP*, **131**, 024401
 Baker, D. N., Blake, J. B., Callis, L. B., et al. 1994, *GeoRL*, **21**, 409
 Baker, D. N., Jaynes, A. N., Li, X., et al. 2014, *GeoRL*, **41**, 1351
 Balogh, A., Bothmer, V., Crooker, N. U., et al. 1999, *SSRv*, **89**, 141
 Bame, S. J., Goldstein, B. E., Gosling, J. T., et al. 1993, *GeoRL*, **20**, 2323
 Belakhovsky, V., Pilipenko, V., Engebretson, M., Sakharov, Y., & Selivanov, V. 2019, *JWSC*, **9**, A18
 Belcher, J. W., & Davis, L. 1971, *JGR*, **76**, 3534
 Berger, T., Matthä, D., Burmeister, S., et al. 2018, *SpWea*, **16**, 1173
 Boteler, D. H. 2003, *NH*, **28**, 537
 Boyd, A. J., Spence, H. E., Claudepierre, S. G., et al. 2014, *GeoRL*, **41**, 2275
 Bruno, A., Christian, E. R., de Nolfo, G. A., Richardson, I. G., & Ryan, J. M. 2019, *SpWea*, **17**, 419
 Burlaga, L., Fitzenreiter, R., Lepping, R., et al. 1998, *JGR*, **103**, 277
 Burlaga, L. F. 1974, *JGR*, **79**, 3717
 Burlaga, L. F., Ness, N. F., Mariani, F., et al. 1978, *JGR*, **83**, 5167
 Burlaga, L. F., Sittler, E., Mariani, F., & Schwenn, R. 1981, *JGR*, **6**, 6673
 Burton, R. K., McPherron, R. L., & Russell, C. T. 1975, *JGR*, **80**, 4204
 Campbell, W. H. 1980, *GeoJI*, **61**, 437
 Chamberlin, P. C., Woods, T. N., Didkovsky, L., et al. 2018, *SpWea*, **16**, 1470
 Chertok, I. M., Belov, A. V., & Abunin, A. A. 2018, *SpWea*, **16**, 1549
 Crooker, N. U., Antiochos, S. K., Zhao, X., & Neugebauer, M. 2012, *JGRA*, **117**, A04104
 Crooker, N. U., Huang, C.-L., Lamassa, S. M., et al. 2004, *JGRA*, **109**, A03107
 Daglis, I. A., Livi, S., Sarris, E. T., & Wilken, B. 1994, *JGR*, **99**, 5691
 Davis, T. N., & Sugiura, M. 1966, *JGR*, **71**, 785
 Davis, L., Jr. 1966, in The Solar Wind, ed. R. J. Mackin, Jr. & M. Neugebauer (New York: Pergamon), 147
 Davis, L., Jr., Smith, E. J., Coleman, P. J., Jr., & Sonnet, C. P. 1966, in The Solar Wind, ed. R. J. Mackin, Jr. & M. Neugebauer (New York: Pergamon), 35
 Domingo, V., Fleck, B., & Poland, A. I. 1995, *SoPh*, **162**, 1
 Dungey, J. W. 1961, *PhRvL*, **6**, 47
 Echer, E., Gonzalez, W. D., & Tsurutani, B. T. 2008, *GeoRL*, **35**, L06S03
 Echer, E., Tsurutani, B. T., & Guarnieri, F. L. 2009, *AdSpR*, **44**, 615
 Echer, E., Tsurutani, B. T., & Guarnieri, F. L. 2010a, *JASTP*, **72**, 280
 Echer, E., Tsurutani, B. T., & Guarnieri, F. L. 2010b, *AdSpR*, **45**, 798
 Fang, X., Randall, C. E., Lummerzheim, D., et al. 2010, *GeoRL*, **37**, L22106
 Farrugia, C. J., Erkaev, N. V., Biernat, H. K., et al. 1997, *JGR*, **102**, 7087
 Forsyth, R. J., & Marsch, E. 1999, *SSRv*, **89**, 7
 Fujita, S., Kataoka, R., Fujii, I., Pulkkinen, A., & Watari, S. 2016, *EP&S*, **68**, 51
 Gjerloev, J. W. 2009, *EosTr*, **90**, 230
 Gonzalez, W. D., Guarnieri, F. L., Clua-Gonzalez, A. L., et al. 2006, in Recurrent Magnetic Storms: Corotating Solar Wind Streams, Geophysical Monograph Series, 167, ed. B. T. Tsurutani et al. (Washington: AGU), 175
 Gonzalez, W. D., Joselyn, J. A., Kamide, Y., et al. 1994, *JGR*, **99**, 5771
 Gosling, J. T., Asbridge, J. R., Bame, S. J., & Feldman, W. C. 1978, *JGR*, **83**, 1401
 Hajra, R., Echer, E., Tsurutani, B. T., & Gonzalez, W. D. 2013, *JGRA*, **118**, 5626
 Hajra, R., Echer, E., Tsurutani, B. T., & Gonzalez, W. D. 2014a, *JGRA*, **119**, 2675
 Hajra, R., Echer, E., Tsurutani, B. T., & Gonzalez, W. D. 2014b, *JASTP*, **121**, 24
 Hajra, R., & Tsurutani, B. T. 2018a, *ApJ*, **858**, 123
 Hajra, R., & Tsurutani, B. T. 2018b, in Extreme Events in Geospace: Origins, Predictability, and Consequences, ed. N. Buzulukova (Amsterdam: Elsevier), 373
 Hajra, R., Tsurutani, B. T., Echer, E., et al. 2015a, *EP&S*, **67**, 109
 Hajra, R., Tsurutani, B. T., Echer, E., & Gonzalez, W. D. 2014c, *GeoRL*, **41**, 1876
 Hajra, R., Tsurutani, B. T., Echer, E., Gonzalez, W. D., & Gjerloev, J. W. 2016, *JGRA*, **121**, 7805
 Hajra, R., Tsurutani, B. T., Echer, E., Gonzalez, W. D., & Santolik, O. 2015b, *ApJ*, **799**, 39
 Horne, R. B., Lam, M. M., & Green, J. C. 2009, *GeoRL*, **36**, L19104
 Horne, R. B., & Thorne, R. M. 1998, *GeoRL*, **25**, 3011
 Hudson, M. K., Baker, D. N., Goldstein, J., et al. 2014, *GeoRL*, **41**, 1113
 Hundhausen, A. J., & Burlaga, L. F. 1975, *JGR*, **80**, 1845
 Illing, R. M. E., & Hundhausen, A. J. 1986, *JGR*, **91**, 10951
 Iyemori, T., & Rao, D. R. K. 1996, *AnGeo*, **14**, 608
 Iyemori, T., Takeda, M., Nose, M., Odagi, Y., & Toh, H. 2010, Mid-latitude Geomagnetic Indices ASY and SYM for 2009 (Provisional), Internal Report of Data Analysis Center for Geomagnetism and Space Magnetism (Japan: Kyoto University), <http://wdc.kugi.kyoto-u.ac.jp/aeasy/asy.pdf>
 Jian, L., Russell, C. T., Luhmann, J. G., & Skoug, R. M. 2006, *SoPh*, **239**, 337
 Jiggins, P., Clavie, C., Evans, H., et al. 2019, *SpWea*, **17**, 99
 Jin, H., Zou, S., Chen, G., et al. 2018, *SpWea*, **16**, 648
 Jones, S. L., Lessard, M. R., Fernandes, P. A., et al. 2009, *JASTP*, **71**, 708
 Kanekal, S. G., Baker, D. N., Henderson, M. G., et al. 2015, *JGRA*, **120**, 7629

- Kennel, C. F., Edmiston, J. P., & Hada, T. 1985, in *Collisionless Shocks in the Heliosphere: A Tutorial Review*, ed. R. G. Stone & B. T. Tsurutani (Washington, D.C.: AGU), 1
- Kessel, R. L., Fox, N. J., & Weiss, M. 2013, *SSRv*, **179**, 531
- Klein, L. W., & Burlaga, L. F. 1982, *JGR*, **87**, 613
- Kozyra, J. U., Criwley, G., Emery, B. A., et al. 2006, in *Recurrent Magnetic Storms: Corotating Solar Wind Streams*, Geophysical Monograph Series, 167, ed. B. T. Tsurutani et al. (Washington: AGU), 319
- Krieger, A. S., Timothy, A. F., & Roelof, E. C. 1973, *SoPh*, **29**, 505
- Lakhina, G. S., Hajra, R., & Tsurutani, B. T. 2020, in *Earth Sciences Series. Encyclopedia of Solid Earth Geophysics*, ed. H. K. Gupta (2nd ed.; Dordrecht: Springer)
- Lemen, J. R., Title, A. M., Akin, D. J., et al. 2012, *SoPh*, **275**, 17
- Lepping, R. P., Szabo, A., Peredo, M., & Hoeksema, J. T. 1996, *GeoRL*, **23**, 1199
- Lepri, S. T., & Zurbuchen, T. H. 2010, *ApJL*, **723**, L22
- Marsal, S., & Torta, J. M. 2019, *SpWea*, **17**, 941
- Marubashi, K. 2000, *AdSpR*, **26**, 55
- Marubashi, K., & Lepping, R. P. 2007, *AnGeo*, **25**, 2453
- Matthiä, D., Meier, M. M., & Berger, T. 2018, *SpWea*, **16**, 977
- Mauk, B. H., Fox, N. J., Kanekal, S. G., et al. 2013, *SSRv*, **179**, 3
- McComas, D. J., Barraclough, B. L., Funsten, H. O., et al. 2000, *JGR*, **105**, 10419
- McPherron, R. L. 1979, *RvGSP*, **17**, 657
- Meng, X., Tsurutani, B. T., & Mannucci, A. J. 2019, *JGRA*, **124**, 3926
- Meurant, M., Gérard, J.-C., Blockx, C., et al. 2005, *JGRA*, **110**, A07228
- Ness, N. F., & Wilcox, J. M. 1964, *PhRvL*, **13**, 461
- Newell, P. T., & Gjerloev, J. W. 2011, *JGRA*, **116**, A12211
- Nykyri, K., Bengtson, M., Angelopoulos, V., Nishimura, Y. T., & Wing, S. 2019, *JGRA*, **124**, 4314
- O'Brien, T. P., Mazur, J. E., & Looper, M. D. 2018, *SpWea*, **16**, 2022
- Odstrcil, D., & Pizzo, V. J. 1999a, *JGR*, **104**, 483
- Odstrcil, D., & Pizzo, V. J. 1999b, *JGR*, **104**, 493
- Ohtani, S. I. 2001, *SSRv*, **95**, 347
- Onsager, T., Grubb, R., Kunches, J., et al. 1996, *Proc. SPIE*, **281**, 2812
- Palmerio, E., Kilpua, E. K. J., Mostl, C., et al. 2018, *SpWea*, **16**, 442
- Piersanti, M., Di Matteo, S., Carter, B. A., Currie, J., & D'Angelo, G. 2019, *SpWea*, **17**, 1241
- Pirjola, R. 2000, *ITPS*, **28**, 1867
- Pirjola, R., & Lehtinen, M. 1985, *AnGeo*, **3**, 485
- Pizzo, V. J. 1985, in *Collisionless Shocks in the Heliosphere: Reviews of Current Research*, Geophysical Monograph Series, 35, ed. B. T. Tsurutani & R. G. Stone (Washington: AGU), 51
- Pulkkinen, A., Bernabeu, E., Thomson, A., et al. 2017, *SpWea*, **15**, 828
- Pulkkinen, A., Viljanen, A., Pajunpää, K., & Pirjola, R. 2001, *JAG*, **48**, 219
- Redmon, R. J., Seaton, D. B., Steenburgh, R., He, J., & Rodriguez, J. V. 2018, *SpWea*, **16**, 1190
- Rees, M. H. 1963, *P&SS*, **11**, 1209
- Rees, M. H. 1964, *P&SS*, **12**, 722
- Reeves, G. D., Spence, H. E., Henderson, M. G., et al. 2013, *Sci*, **341**, 991
- Richardson, I. G. 2018, *LRSP*, **15**, 1
- Rostoker, G. 2002, *JGRA*, **107**, A7
- Royal Academy of Engineering Report 2013, *Extreme space weather impacts on engineered systems and infrastructure* (London: Royal Academy of Engineering), <https://www.raeng.org.uk/publications/reports/space-weather-full-report>
- Schillings, A., Nilsson, H., Slapak, R., et al. 2018, *SpWea*, **16**, 1363
- Schwenn, R. 1990, in *Physics and Chemistry in Space—Space and Solar Physics*, 20, *Physics of the Inner Heliosphere I*, ed. R. Schwenn & E. Marsch (Berlin: Springer), 99
- Scolini, C., Chané, E., Temmer, M., et al. 2020, *ApJ*, **247**, 21
- Seaton, D. B., & Darnel, J. M. 2018, *ApJL*, **852**, L9
- Semeter, J., & Kamalabadi, F. 2005, *RaSc*, **40**, RS2006
- Sheeley, N. R., & Harvey, J. W. 1981, *SoPh*, **70**, 237
- Smith, E. J. 1985, in *Collisionless Shocks in the Heliosphere: Reviews of Current Research*, Geophysical Monograph Series, 35, ed. B. T. Tsurutani & R. G. Stone (Washington: AGU), 69
- Smith, E. J., Tsurutani, B. T., & Rosenberg, R. L. 1978, *JGR*, **83**, 717
- Smith, E. J., & Wolfe, J. H. 1976, *GeoRL*, **3**, 137
- Sugiura, M. 1964, *Hourly Values of Equatorial Dst for the IGY*, Annual International Geophysical Year, Vol. 35 (New York: Pergamon), 9, <https://ntrs.nasa.gov/archive/nasa/casi.ntrs.nasa.gov/19650020355.pdf>
- Summers, D., Ni, B., & Meredith, N. P. 2007, *JGRA*, **112**, A04207
- Tang, F., Tsurutani, B. T., Gonzalez, W. D., Akasofu, S. I., & Smith, E. J. 1989, *JGR*, **94**, 3535
- Tsurutani, B. T., Arballo, J. K., Lakhina, G. S., et al. 1998, *JGRA*, **25**, 3047
- Tsurutani, B. T., Echer, E., & Gonzalez, W. D. 2011, *AnGeo*, **29**, 839
- Tsurutani, B. T., & Gonzalez, W. D. 1987, *P&SS*, **35**, 405
- Tsurutani, B. T., & Gonzalez, W. D. 1997, in *Magnetic Storms*, 98, ed. B. T. Tsurutani et al. (Washington: AGU), 77
- Tsurutani, B. T., Gonzalez, W. D., Gonzalez, A. L. C., et al. 1995, *JGR*, **100**, 21717
- Tsurutani, B. T., Gonzalez, W. D., Gonzalez, A. L. C., et al. 2006a, *JGRA*, **111**, A07S01
- Tsurutani, B. T., Gonzalez, W. D., Tang, F., Akasofu, S. I., & Smith, E. J. 1988, *JGR*, **93**, 8519
- Tsurutani, B. T., Gonzalez, W. D., Zhou, X. Y., Lepping, R. P., & Bothmer, V. 2004a, *JASTP*, **66**, 147
- Tsurutani, B. T., Hajra, R., Echer, E., & Gjerloev, J. W. 2015, *AnGeo*, **33**, 519
- Tsurutani, B. T., Hajra, R., Tanimori, T., et al. 2016, *JGRA*, **121**, 10130
- Tsurutani, B. T., & Lin, R. P. 1985, *JGR*, **90**, 1
- Tsurutani, B. T., McPherron, R. L., Gonzalez, W. D., et al. 2006b, in *Recurrent Magnetic Storms: Corotating Solar Wind Streams*, Geophysical Monograph Series, 167, ed. B. T. Tsurutani et al. (Washington: AGU), 1
- Tsurutani, B. T., & Meng, C. I. 1972, *JGR*, **77**, 2964
- Tsurutani, B. T., Wu, S. T., Zhang, T. X., & Dryer, M. 2003a, *A&A*, **412**, 293
- Tsurutani, B. T., Zhou, X., Gonzalez, W. D., & Guarnieri, F. L. 2004b, in *Substorms-7: Proceedings of the 7th International Conference on Substorms*, ed. N. Ganushkina & T. I. Pulkkinen (Helsinki: Finnish Meteorological Institute), 63
- Tsurutani, B. T., Zhou, X. Y., & Gonzalez, W. D. 2003b, in *Disturbances in Geospace: The Storm-Substorm Relationship*, Geophysical Monograph Series, 142, ed. A. S. Sharma, Y. Kamide, & G. S. Lakhina (Washington: AGU), 23
- Turner, N. E., Mitchell, E. J., Knipp, D. J., & Emery, B. A. 2006, in *Recurrent Magnetic Storms: Corotating Solar Wind Streams*, Geophysical Monograph Series, 167, ed. B. T. Tsurutani et al. (Washington: AGU), 113
- Van Allen, J. A., & Frank, L. A. 1959, *Natur*, **184**, 219
- Viljanen, A., Nevanlinna, H., Pajunpää, K., & Pulkkinen, A. 2001, *AnGeo*, **19**, 1107
- Viljanen, A., Pulkkinen, A., Pirjola, R., et al. 2006, *SpWea*, **4**, S10004
- von Steiger, R., Geiss, J., & Gloeckler, G. 1997, in *Cosmic Winds and the Heliosphere*, ed. J. R. Jokipii, C. P. Sonett, & M. S. Giampapa (Arizona: Univ. Arizona Press), 581
- Wanliss, J. A., & Showalter, K. M. 2006, *JGRA*, **111**, A02202
- Werner, A. L. E., Yordanova, E., Dimmock, A. P., & Temmer, M. 2019, *SpWea*, **17**, 357
- West, H. I., Buck, R. M., & Walton, J. R. 1972, *Natur*, **240**, 6
- Wimmer-Schweingruber, R. E., von Steiger, R., & Paerli, R. 1997, *JGR*, **102**, 17407
- Winterhalter, D., Smith, E. J., Burton, M. E., Murphy, N., & McComas, D. J. 1994, *JGR*, **99**, 6667
- Yan, X. L., Wang, J. C., Pan, G. M., et al. 2018, *ApJ*, **856**, 79
- Yurchyshyn, V., Hu, Q., Lepping, R. P., Lynch, B. J., & Krall, J. 2007, *AdSpR*, **40**, 1821
- Zhang, J., Richardson, I. G., Webb, D. F., et al. 2007, *JGRA*, **112**, A10102
- Zhou, X., & Tsurutani, B. T. 2001, *JGR*, **106**, 18957
- Zou, P., Jiang, C., Feng, X., et al. 2019, *ApJ*, **870**, 97
- Zurbuchen, T. H., & Richardson, I. G. 2006, *SSRv*, **123**, 31